nature materials

ARTICLES

https://doi.org/10.1038/s41563-019-0378-4

Molecular optical imaging probes for early diagnosis of drug-induced acute kidney injury

Jiaguo Huang, Jingchao Li, Yan Lyu, Qingqing Miao and Kanyi Pu*

Drug-induced acute kidney injury (AKI) with a high morbidity and mortality is poorly diagnosed in hospitals and deficiently evaluated in drug discovery. Here, we report the development of molecular renal probes (MRPs) with high renal clearance efficiency for in vivo optical imaging of drug-induced AKI. MRPs specifically activate their near-infrared fluorescence or chemiluminescence signals towards the prodromal biomarkers of AKI including the superoxide anion, *N*-acetyl-β-D-glucosaminidase and caspase-3, enabling an example of longitudinal imaging of multiple molecular events in the kidneys of living mice. Importantly, they in situ report the sequential occurrence of oxidative stress, lysosomal damage and cellular apoptosis, which precedes clinical manifestation of AKI (decreased glomerular filtration). Such an active imaging mechanism allows MRPs to non-invasively detect the onset of cisplatin-induced AKI at least 36 h earlier than the existing imaging methods. MRPs can also act as exogenous tracers for optical urinalysis that outperforms typical clinical/preclinical assays, demonstrating their clinical promise for early diagnosis of AKI.

Acute kidney injury (AKI) manifests as a rapid decline in renal function and is a significant health issue including a high morbidity and mortality with an estimated 1.7 million deaths per year globally[1]. The main etiologies of AKI include sepsis, ischaemia/reperfusion and nephrotoxin exposure[2,3]. Among them, nephrotoxicity underlies up to 25% of AKI cases due to the use of clinically approved drugs[4]. The morbidity of drug-induced AKI can be reduced via a safer pharmacopeia and/or close monitoring of renal function during the use of known nephrotoxic drugs[5]. In particular, early detection of kidney injury at the incipient stage can allow renoprotective intervention to be conducted in a timely manner to prevent AKI from progressing into more severe complications including chronic kidney disease, renal replacement therapy and death, and aid in kidney recovery[6]. However, drug-induced AKI is deficiently evaluated in drug discovery due to the limitations of in vitro assays[5]. Moreover, current clinical diagnostic methods cannot identify AKI early because they often rely on the measurement of serum creatinine (sCr) and blood urea nitrogen (BUN)[7], which are insensitive indicators of late-stage renal dysfunction[8]. Therefore, drug-induced AKI will probably remain a clinical inevitability due to the increased use of prescription drugs and aggressive pharmacomedical management[9].

Molecular imaging is a non-invasive way to detect the onset and progression of diseases in real-time in living organisms[10–13]. It has promise for in situ longitudinal monitoring of molecular events in kidneys, which is difficult for in vitro diagnostic methods based on static analysis. While single-photon emission computed tomography, contrast-enhanced computed tomography, magnetic resonance imaging and ultrasonography are used routinely for kidney imaging, they mainly detect anatomic and functional changes of organs and have little utility in detecting the early-stage molecular-level changes that underlie AKI[14]. In contrast, optical imaging offers high spatiotemporal resolution and superb sensitivity[15–18] and can measure subtle changes in biomarker concentrations at the disease site via molecular probes[19,20]. However, real-time in vivo optical imaging of drug-induced AKI has yet to be demonstrated.

Identification of early biomarkers and development of related molecular probes are crucial for early diagnosis of drug-induced AKI. Previously, the lysosomal enzyme *N*-acetyl-beta-D-glucosaminidase (NAG)[21], inflammatory mediators (trefoil factor-3 (TFF3)[22], osteopontin (OPN)[23] and neutrophil gelatinase-associated lipocalin (NGAL)[24]), glomerular filtration markers (cystatin-C (Cyst C)[24] and β2-microglobulin (β2-Mic)[24]) and other upregulated structural proteins (kidney injury molecule-1 (KIM-1)[21] and clusterin (Clust)[24]) were qualified by the Food and Drug Administration as safety biomarkers for detection of kidney injury. In addition, reactive oxygen species (ROS) have been well reported to be associated with AKI, and dysregulation of ROS can trigger the pathways towards lysosomal damage, cellular apoptosis, necrosis and renal fibrosis[25]. Moreover, many in vitro reports have shown that ROS-induced by-products (isoprostanes, malondialdehyde, oxidized proteins and others)[26] and inflammatory mediators (NGAL, OPN and interleukin-18 (IL-18) and others) are dysregulated in plasma/urine before a substantial increase in sCr/BUN[27]. The fact that both ROS-induced by-products and inflammatory mediators are generated downstream of oxidative stress implies that direct ROS detection could identify AKI earlier.

We report here the development of optical molecular renal probes (MRPs) for real-time imaging of early-stage biomarkers in murine models of drug-induced AKI. These probes comprise three key building blocks (Fig. 1): a renal clearance moiety, a biomarker reactive moiety and a luminescent signalling moiety. Molecular screening found that (2-hydroxypropyl)-β-cyclodextrin (HPβCD) could dramatically facilitate probe renal clearance with an efficacy above 97%. The superoxide anion ($O_2^{\bullet-}$), NAG and caspase-3 are selected as the target AKI biomarkers because they are related to oxidative stress, lysosomal damage and cellular apoptosis, respectively. MRPs1–3 (Fig. 1) are single-channel probes that turn on their near-infrared fluorescence (NIRF) in the presence of these three respective biomarkers. MRP_D (Fig. 1) is a dual-channel probe that is always fluorescent but becomes chemiluminescent only after reaction with $O_2^{\bullet-}$. The fluorescent MRPs offer imaging of three interlinked molecular events in the kidneys to identify the earliest

School of Chemical and Biomedical Engineering, Nanyang Technological University, Singapore, Singapore. *e-mail: kypu@ntu.edu.sg

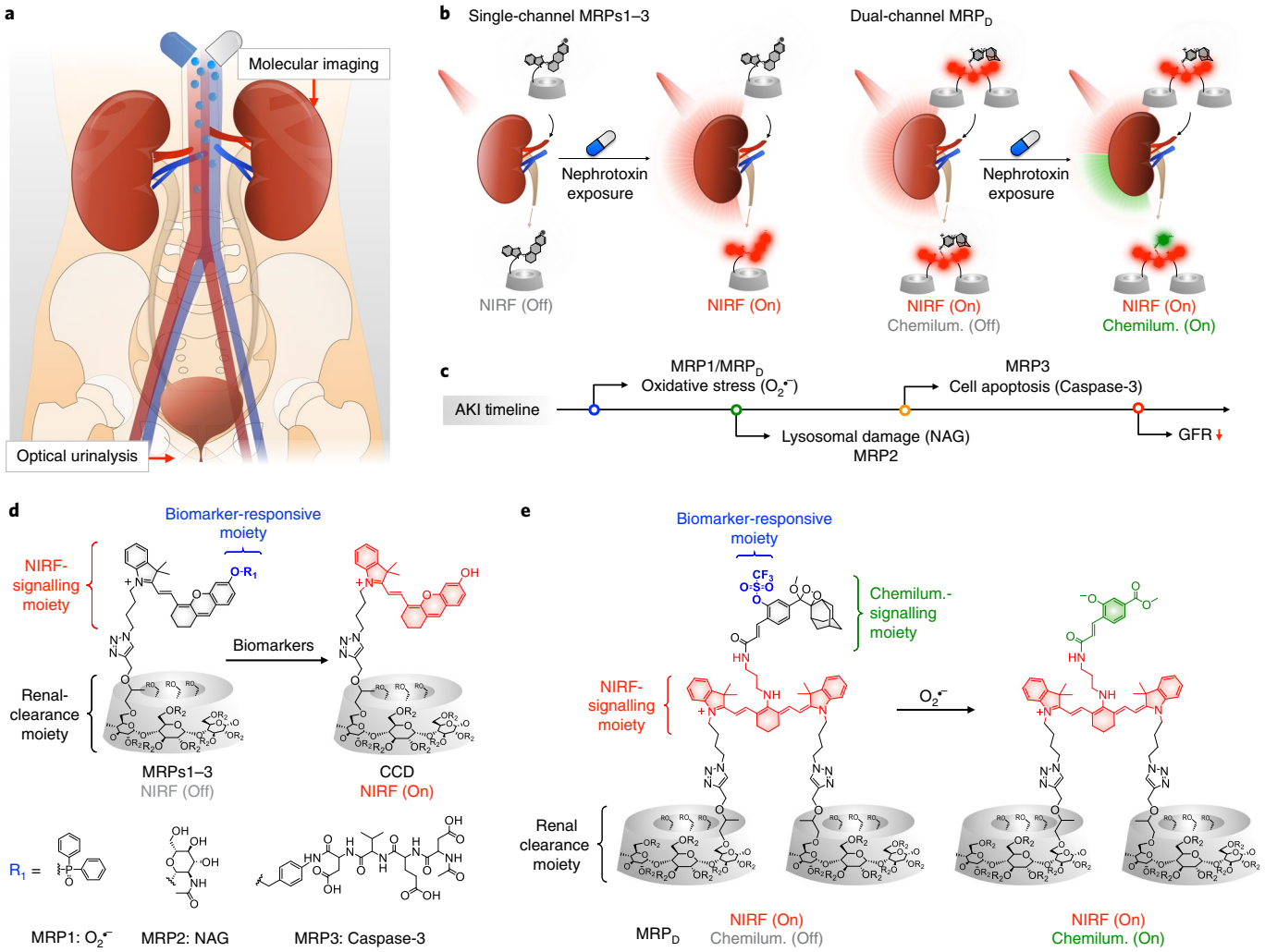

Fig. 1 | Design and mechanisms of MRPs for molecular imaging and early detection of drug-induced AKI a, A schematic of drug-induced AKI and the AKI detection methods used here including molecular imaging and optical urinalysis. **b**, Real-time non-invasive imaging of drug-induced AKI using the single-channel NIRF turn-on MRPs1–3 and the dual-channel chemiluminescent MRP$_D$. **c**, A timeline of AKI comparing the molecular events including oxidative stress, lysosomal damage and cell apoptosis with the decrease in GFR. **d**, Chemical structures of MRPs1–3 and their activated form as CCD in response to their respective biomarkers ($O_2^{\bullet-}$ for MRP1, NAG for MRP2 and caspase-3 for MRP3). **e**, Chemical structures of MRP$_D$ and its activated form in response to $O_2^{\bullet-}$ (R_2 = H or $CH_2CHOHCH_3$).

predictor for AKI. MRP$_D$ enables simultaneous monitoring of $O_2^{\bullet-}$ and probe clearance via the chemiluminescent and NIRF signals, respectively, providing the feasibility to directly compare the time between upregulation of $O_2^{\bullet-}$ and changes in glomerular filtration after nephrotoxic exposure in living animals.

Synthesis and in vitro detection

The MRPs were synthesized via a convergent approach (Supplementary Figs. 1 and 2). The fluorescent MRPs (MRPs1–3) were constructed on a hemi-cyanine precursor (CyOH) with an aromatic hydroxyl group and an azide group on the alkyl chain linked to the indole ring (Supplementary Fig. 1 and Methods). The hydroxyl group of CyOH was first caged with diphenylphosphinyl, *N*-acetyl-*β*-D-glucosaminide or a tetrapeptide sequence (Asp-Glu-Val-Asp: Ac-DEVD) (Supplementary Fig. 3 and Methods), which could be specifically cleaved by $O_2^{\bullet-}$, NAG and caspase-3, respectively. The azide group of CyOH was then conjugated with the alkyne-functionalized HPβCD via a click reaction. MRP$_D$ was synthesized from an uncaged fluorescent heptamethine cyanine dye (Cy7NH2) (Supplementary Fig. 2 and Methods), which has two azide groups on the alkyl chain linked to the indole ring and an alkyl amine on the *meso* position. The amine group of Cy7NH2 was first coupled with the caged chemiluminescent phenoxy-dioxetane substrate stabilized by a $O_2^{\bullet-}$-cleavable trifluoromethanesulfonate group on the phenol position. The azide groups were then reacted with the alkyne-functionalized HPβCD to afford MRP$_D$.

MRPs1–3 had similar optical profiles with an absorption maximum at ~600 nm and were barely fluorescent at the intrinsic state (Fig. 2a–c). This was because they were 'caged' wherein the electron-donating ability of the aromatic hydroxyl group was inhibited by the substituents[28]. The absorption spectra of MRPs1–3 changed in respond to their respective biomarkers with a peak shift to 695 nm; meanwhile, the fluorescence at 720 nm (Fig. 2e–g) increased by 21, 19 and 17-fold for MRP1, MRP2 and MRP3, respectively. The optical profiles of these probes resembled the uncaged derivative (HPβCD-substituted CyOH (CCD)) (Supplementary Fig. 4a), which had an unsubstituted hydroxyl group liberating the strong electron-donating ability of the phenolate group on the fluorophores. High-performance liquid chromatography (HPLC) analysis (Supplementary Fig. 4) confirmed the rapid cleavage of the

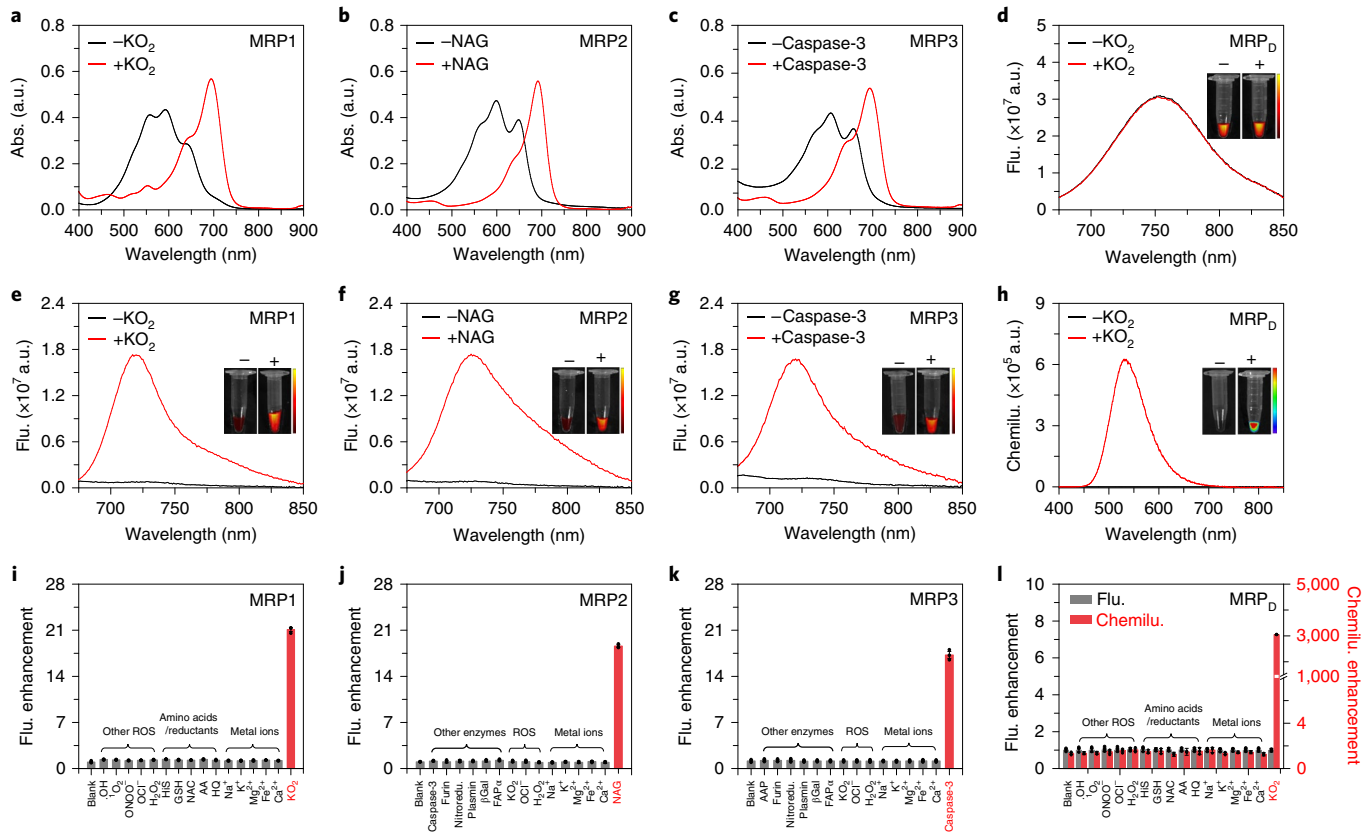

Fig. 2 | In vitro evaluation of the sensing capabilities of the MRPs. a–c,e–g, Absorption (**a–c**) and fluorescence spectra (**e–g**) of MRPs1–3 (30 μM) in the absence or presence of their respective biomarkers (60 μM KO_2, 40 mU NAG and 0.5 μg caspase-3, respectively) in PBS (10 mM, pH 7.4) at 37 °C. The fluorescence excitation was set at 675 nm. Insets: the corresponding fluorescence images acquired at 720 nm following excitation at 675 nm with the IVIS spectrum imaging system. **d,h**, Fluorescence (**d**) and chemiluminescence spectra (**h**) of MRP_D (30 μM) in the absence or presence of KO_2 (60 μM) in PBS (10 mM, pH 7.4) at 37 °C. The fluorescence excitation was set at 640 nm. Insets: the corresponding fluorescence images acquired at 760 nm following excitation at 640 nm and chemiluminescence images acquired under bioluminescence mode with an acquisition time of 1 s. The experiments (**a–h**) were repeated independently three times with similar results. **i–k**, The NIRF changes of MRPs1–3 (30 μM) at 720 nm after incubation with the indicated ROS (150 μM), enzymes and other analytes (150 μM) in PBS (10 mM, pH 7.4) at 37 °C. **l**, NIRF (760 nm) and chemiluminescence changes (540 nm) of MRP_D (30 μM) after incubation with the indicated ROS (150 μM) and other analytes (150 μM) in PBS (10 mM, pH 7.4) at 37 °C. The fluorescence excitation was set at 640 nm and the chemiluminescence was acquired under bioluminescence mode with an acquisition time of 1 s. The data are the mean ± s.d. $n = 3$ independent experiments. •OH, hydroxyl radical; $ONOO^-$, peroxynitrite; GSH, glutathione; His, histidine; AA, ascorbic acid; HQ, hydroquinone; NAC, *N*-acetyl-L-cysteine; Nitroredu., nitroreductase; βGal, β-galactosidase; FAPα, fibroblast activation protein-α; AAP, alanine aminopeptidase.

responsive moieties in MRPs1–3 by their respective biomarkers. The limit of detection (LOD) for MRP1 against $O_2^{\bullet-}$ was 11 nM (Supplementary Fig. 4b–d); the catalytic efficiencies (K_{cat}/K_m) of NAG towards MRP2 (and caspase-3 towards MRP3) were calculated to be 0.17 (and 0.86) $\mu M^{-1} s^{-1}$, respectively (Supplementary Fig. 4e,f and Table 1). In contrast, the fluorescence intensities of MRPs1–3 showed only neglectable fluorescence increases towards the interfering substances including other enzymes, ROS and metal ions (Fig. 2i–k), confirming their high specificity.

In contrast to the turn-on fluorescent response of MRPs1–3, the fluorescence of MRP_D was always on and inert to the tested biological molecules (Fig. 2d). MRP_D had a chemiluminescent phenoxy-dioxetane unit whose activity was initially inhibited due to the presence of trifluoromethanesulfonate substitution on its phenol group. In the presence of $O_2^{\bullet-}$, nucleophilic attack occurred on the sulfonate ester group of MRP_D, leading to the cleavage of trifluoromethanesulfonate and formation of a phenolate dioxetane intermediate (Supplementary Fig. 5). This unprotected intermediate was unstable and spontaneously underwent a chemically initiated electron-exchange luminescence process[29], resulting in chemiluminescence at 540 nm. Addition of $O_2^{\bullet-}$ to MRP_D led to a 3,000-fold increase in the chemiluminescent signal (Fig. 2h), which was not observed with other substances (Fig. 2l). The LOD for MRP_D against $O_2^{\bullet-}$ (13 nM) was similar to that for MRP1, and its chemiluminescence half-life (8.9 min) was sufficient for in vivo imaging (Supplementary Fig. 6). Note that, despite the presence of the NIR-emissive unit in MRP_D, the chemiluminescence maximum was the same as for the dioxetane unit itself (540 nm), suggesting little energy transfer between the chemiluminescent unit and the NIR unit, probably because of their long distance. This chemiluminescence was detected through 1.5 cm of chicken tissue (Supplementary Fig. 6e–h), confirming its utility for in vivo imaging.

Renal clearance and in vivo stability studies

The biodistribution of MRPs was studied and compared with that of their uncaged derivatives including the methyl-substituted hemicyanine skeleton (CMe), the HPβCD-substituted CyOH (CCD) and the poly(ethylene glycol) (PEG)-substituted CyOH (CP2 and CP5 with PEG2000 and PEG5000, respectively) (Fig. 3a). As the uncaged derivatives and MRP_D were intrinsically fluorescent (Supplementary Table 2), NIRF imaging was used to track their biodistribution after intravenous (i.v.) administration. Fluorescence signals were quickly

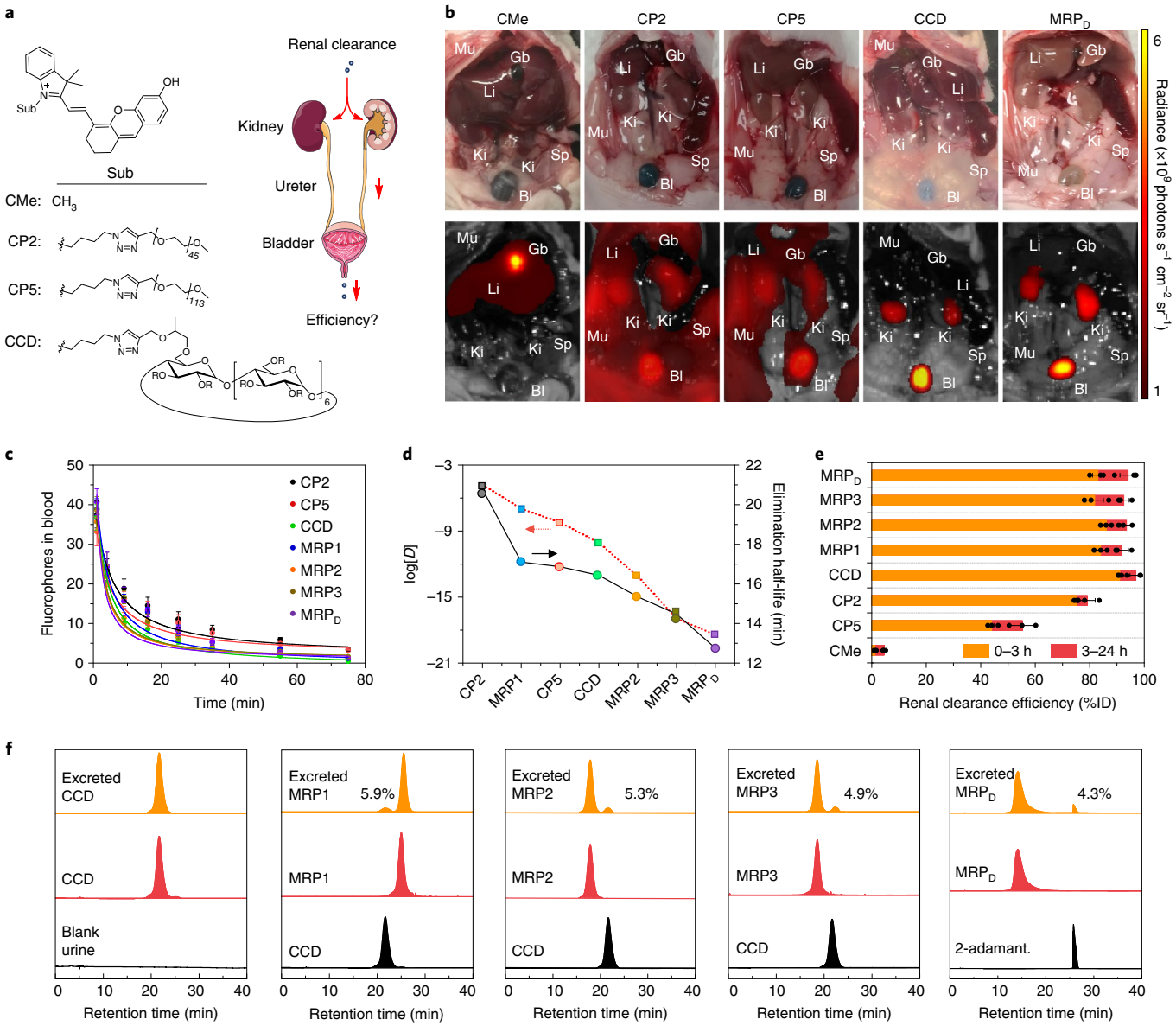

Fig. 3 | Renal clearance and in vivo stability studies of MRPs and the uncaged fluorophores. a, The chemical structures of CMe, CP2, CP5 and CCD (R = H or $CH_2CHOHCH_3$) and a schematic illustration of the excretion of renal-clearable probes through the urinary tract. **b**, NIRF images of the abdominal cavity of mice at $t = 60$ min after i.v. injection of CMe, CP2, CP5, CCD or MRP_D. Bl, bladder; Gb, gallbladder; Ki, kidneys; Li, liver; Mu, muscle; Sp, spleen. The NIRF images were acquired at 720 nm (760 nm for MRP_D) following excitation at 675 nm (640 nm for MRP_D) with the IVIS spectrum imaging system. **c**, Blood concentration (%ID g^{-1}) decay of the uncaged fluorophores (CP2, CP5 and CCD) and MRPs after i.v. injection into living mice. The data are the mean ± s.d. $n = 3$ independent mice. **d**, The correlation between elimination half-life and distribution coefficient (log[*D*]) for the uncaged fluorophores (CP2, CP5 and CCD) and MRPs. **e**, The renal clearance efficiency of the uncaged fluorophores (CMe, CP2, CP5 and CCD) and MRPs at 0–3 h and 3–24 h after i.v. injection. The data are the mean ± s.d. $n = 3$ independent mice. **f**, In vivo stability studies of CCD and MRPs through HPLC analysis of excreted components in the urine samples after i.v. injection. HPLC traces of the pure compounds (CCD, MRPs and 2-adamantanone) are also shown for comparison. The experiments in **b** and **f** were repeated independently three times with similar results.

detected for CCD and MRP_D in the kidneys and bladder 30 min post-injection (Supplementary Fig. 7a); this was not seen for CP2, CP5 and CMe in the whole-body images.

Ex vivo NIRF imaging of the abdominal cavity of mice (Fig. 3b) and biodistribution data (Supplementary Fig. 7b,c) at 1 h post-injection showed that CCD and MRP_D mainly accumulated in the kidneys and bladder. The signals in other organs were close to the background of saline-treated mice. In contrast, CP2 and CP5 had a relatively high accumulation in the gallbladder, liver, lung and muscle in addition to the kidneys and bladder; CMe was trapped by the reticuloendothelial system and mainly accumulated in the liver, gallbladder and intestine. Thus, the ex vivo data revealed that although both PEG- and HPβCD-substituted CyOH could be excreted through the kidney, the relatively high uptake in other organs for CP2 and CP5 caused signal interference limiting kidney visualization in the real-time whole-body images.

HPLC was used to study fluorophore pharmacokinetics by quantifying the fluorophores in the blood and urine of living mice as a function of time after i.v. injection. The probe concentration in the blood decreased close to 0% injected doses (ID) g^{-1} at 75 min

post-injection for all fluorophores (Fig. 3c). The elimination half-lives ($t_{1/2\beta}$) of the HPβCD-substituted fluorophores (<17 min) were shorter than for CP2 (20.8 min) (Supplementary Table 3). Furthermore, the trend of $t_{1/2\beta}$ was generally consistent with their distribution coefficients (log[D]) (Fig. 3d), implying that hydrophilicity played a role in their blood elimination. Urine analysis showed that the renal clearance efficiencies of the HPβCD-substituted fluorophores were higher than others (Fig. 3e and Supplementary Fig. 8). These were determined to be >80% ID at 3 h post-injection and >92% ID at 24 h post-injection (92 ± 2.1, 94 ± 2.2, 93 ± 2.0, 94 ± 3.0 and 97 ± 2.7% ID for MRP1, MRP2, MRR3, MRP_D and CCD, respectively). In contrast, CP2 and CP5 reached only 79 ± 3 and 55 ± 5% ID at 24 h post-injection, respectively, and CMe was nearly undetectable in urine due to reticuloendothelial system uptake. The highly efficient renal clearance of MRPs is attributed to their relatively low molecular weights (<50 kDa, below the glomerular filtration cutoff) and high hydrophilicity.

To determine in vivo stability, the optical and chemical profiles of MRPs recovered from the urine of living mice were measured and compared with those of the pure compounds. Except CMe (unable to be recovered from urine), none of the fluorophores from the urine had obvious changes to its absorption and fluorescence spectra after circulation in living mice (Supplementary Fig. 9). Although matrix-assisted laser desorption/ionization (MALDI) analysis validated their intact chemical structures (Supplementary Fig. 10), HPLC quantification (Fig. 3f) identified some CCDs and adamantanone (<6%) from the urine of MRPs1–3- and MRP_D-treated mice, respectively. This is probably due to probe activation by basal levels of biomarkers in healthy mice. These data not only showed that MRPs had minimal in vivo metabolism in healthy mice but also confirmed that their renal clearance efficiencies were near 100% ID for MRPs. In view of the undetectable signals in the major organs at 24 h post-injection of MRPs (Supplementary Fig. 8j,l), MRPs could be considered as fully renal clearable (>97% ID). In addition, histological and immunofluorescence staining revealed that MRPs did not induce cellular apoptosis or cause any tissue damage (Supplementary Fig. 11).

Real-time NIRF imaging

The ability of MRPs1–3 to detect drug-induced AKI was tested in living mice treated with cisplatin (an antineoplastic drug), gentamicin (an antibiotic) or diatrizoate (a radiocontrast agent)—all with known nephrotoxicity[30–32]. Cisplatin was intraperitoneally administered into living mice at a nephrotoxic dosage (Fig. 4a and Methods), followed by i.v. injection of MRPs at different time points post-treatment with cisplatin (8, 12, 16, 24 and 48 h). The control groups were treated with saline or a nephroprotective antioxidant (*N*-acetyl-L-cysteine (NAC)) before cisplatin administration. Longitudinal NIRF imaging was then conducted for those groups with different drug post-treatment times. At 8 h post-treatment with cisplatin, the signals from MRPs1–3 in the kidneys were as low as those of the control mice (Fig. 4b–d and Supplementary Fig. 12). However, at 12 h post-treatment with cisplatin, the injection of MRP1 led to a gradual signal increase in the kidneys with a signal maximum 30 min post-injection of MRP1 (Fig. 4e; 1.45-fold higher than in control mice). The MRP1 signals in the kidneys and bladder decreased at later imaging time points due to its short elimination half-life. Similar trends were observed for MRP2 and MRP3, but the earliest time points that they showed a statistically significant signal increase were 16 and 48 h post-treatment with cisplatin for MRP2 (1.56-fold) and MRP3 (1.60-fold), respectively (Fig. 4f and Supplementary Fig. 12). This sequential activation suggested that cisplatin first induced oxidative stress followed by lysosomal damage and cellular apoptosis. The maximum NIRF signals of MRPs1 and 2 in the kidneys increased with post drug treatment time (Fig. 4f), indicating the gradual upregulation of those biomarkers during the progression of AKI.

Consistent with the in vivo imaging data, whole kidney section imaging revealed that the NIRF signals (Fig. 4g and Supplementary Fig. 13) were detected in the cortex and the outer medulla area for MRP1, MRP2 and MRP3 at 12, 16 and 48 h post-treatment with cisplatin, respectively. The caspase-3 signal was detectable only at 48 h post-treatment with cisplatin, and the histological staining (Fig. 4h and Supplementary Fig. 13k) showed normal tubular morphology at 48 h post-treatment with cisplatin, but loss of the brush border and hyaline casts at 72 h post-treatment with cisplatin. Magnified regional kidney section imaging further clarified that the NIRF signals of activated MRPs1–3 mainly came from the renal tubules rather than the glomeruli (Fig. 4i). This was because the tubules are at the frontline of nephrotoxin clearance; tubular injury is well reported for nephrotoxin exposure[33]. Thus, these data further validated that $O_2^{\bullet-}$, NAG and caspase-3 were sequentially upregulated before injury of kidney tissue. They also revealed that these molecular events occurred in renal tubules after nephrotoxin exposure. Note that similar trends were observed for the signal increases of MRPs1 and 2 in the mouse model of gentamicin- or diatrizoate-induced AKI (Supplementary Figs. 14–17).

Real-time independent dual-channel imaging

To confirm that MRPs could predict drug-induced AKI before the change in glomerular filtration, the dual-channel probe (MRP_D) was intravenously injected into living mice at different post drug treatment times (8, 12, 48 and 72 h). Longitudinal chemiluminescence and NIRF imaging were simultaneously conducted. At 8 h post-treatment with cisplatin, the chemiluminescent signal of MRP_D in the kidneys was close to the background (Fig. 5a and Supplementary Fig. 18), but the NIRF signal was detected (Fig. 5b; always-on signal). The NIRF signal reached a maximum at 8 min post-injection of MRP_D and then decreased with time (Fig. 5e). At 12 h post-treatment with cisplatin, the chemiluminescent signal was detected in the kidney, 14.6-fold higher than that of the control at 8 min post-injection of MRP_D. Moreover, similar chemiluminescent

Fig. 4 | Real-time in vivo NIRF imaging of cisplatin-induced AKI. a, A schematic illustration of the development of the cisplatin (20 mg kg^{-1} body weight)-induced AKI mouse model and NIRF imaging at different post-treatment time points. **b**–**d**, Representative NIRF images of living mice after i.v. injection of MRP1 (**b**), MRP2 (**c**) or MRP3 (**d**) at different post-treatment time points (8, 12, 16, 24 or 48 h). The white arrows indicate the kidneys and bladder in the dorsal and ventral side, respectively. **e**, The dynamic NIRF intensities of kidneys as a function of time post-injection of MRPs1–3 in living mice after treatment with cisplatin for 12 h. The data are the mean ± s.d.; $n = 3$ independent mice; two-tailed Student's t-test; saline, NAC/cisplatin versus cisplatin-treated groups, NS: not significant, $^*P < 0.05$. **f**, NIRF intensities of kidneys in living mice $t = 30$ min after i.v. injection of MRP1 or 60 min after i.v. injection of MRPs2 and 3 at the different post-treatment time points (8, 12, 16, 24 or 48 h). The data are the mean ± s.d.; $n = 3$ independent mice; two-tailed Student's t-test; saline, NAC/cisplatin versus cisplatin-treated groups, NS: not significant, $^*P < 0.05$, $^{**}P < 0.01$, $^{***}P < 0.001$. **g**, Representative confocal fluorescence microscopy images of whole kidney slices from mice with i.v. injection of MRP1, MRP2 and MRP3 at $t = 12$, 16 and 48 h post-treatment with cisplatin, respectively. Scale bars, 2 mm. **h**, Representative photomicrographs of haematoxylin and eosin (H&E) staining in paraffin-embedded kidney sections from mice 12, 16 or 48 h after cisplatin treatment. Scale bar, 50 μm. **i**, Representative confocal fluorescence microscopy images of regional kidney slices from mice with i.v. injection of MRP1, MRP2 and MRP3 at $t = 12$, 16 and 48 h post-treatment with cisplatin, respectively. G, glomerulus; T, tubules; A, arteriole; PC, peritubular capillaries. Scale bars, 40 μm. The experiments in **b–d** and **g–i** were repeated independently three times with similar results.

signal evolution as a function of imaging time was observed for the mouse groups at 12, 48 and 72 h post-treatment with cisplatin (Fig. 5d); however, the maximum chemiluminescent signal of the kidneys at 72 h post-treatment with cisplatin was 1.27- and 1.66-fold higher than that at 48 and 12 h, respectively. This proportional correlation between the maximum chemiluminescent signal and the post-treatment time was consistent with the data acquired with MRP1, confirming that the level of $O_2^{\bullet-}$ was gradually upregulated after drug treatment. In contrast, the maximum NIRF signals of the kidneys had a nonlinear relation with post-treatment time, and a threshold was observed. The profile for the signal as a function of imaging time remained similar when the post-treatment time was no more than 48 h; it changed dramatically at 72 h post-treatment. Instead of a gradually decreasing signal 8 min after injection of MRP_D, the signal was stable, indicating probe retention in the kidneys.

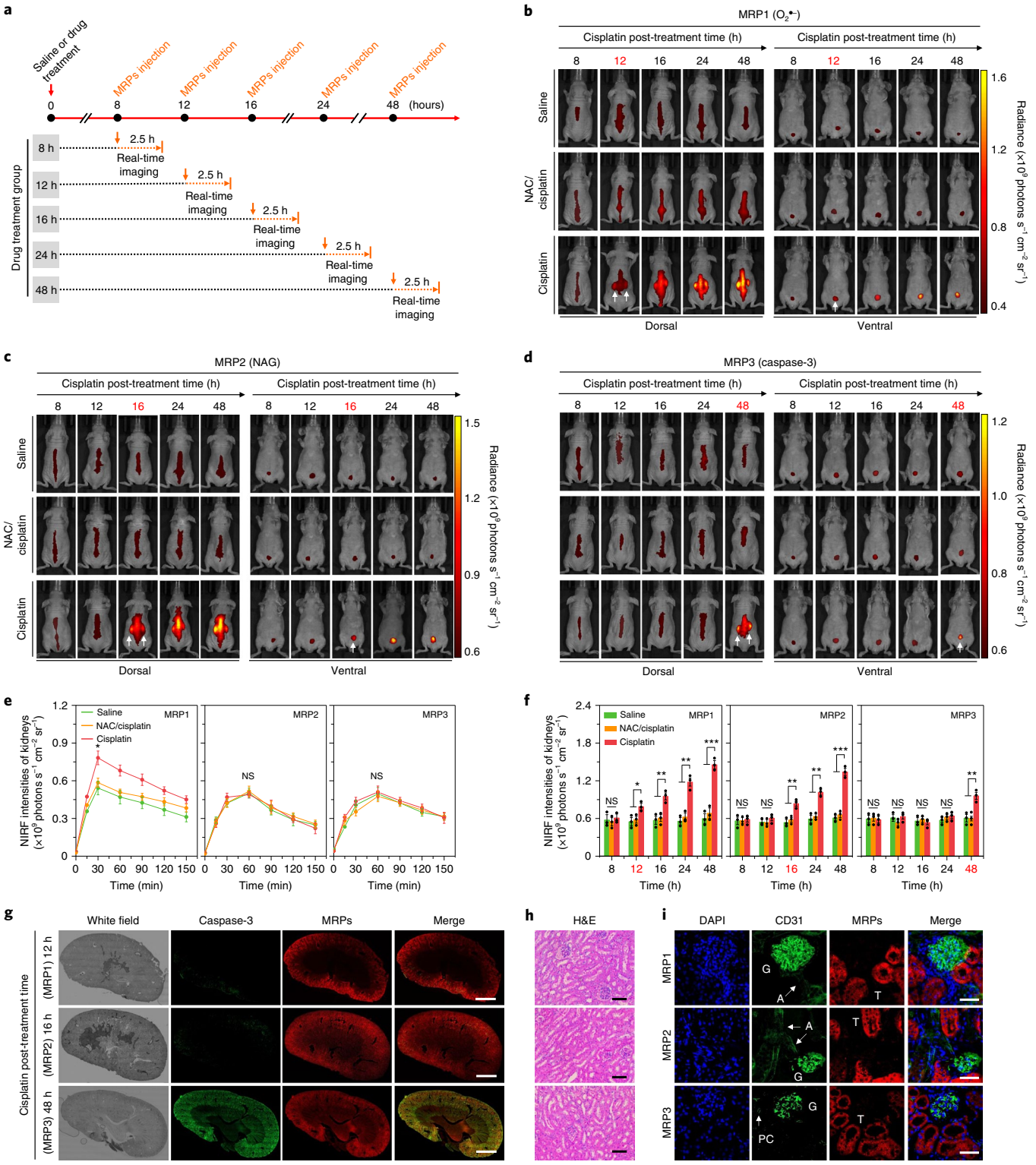

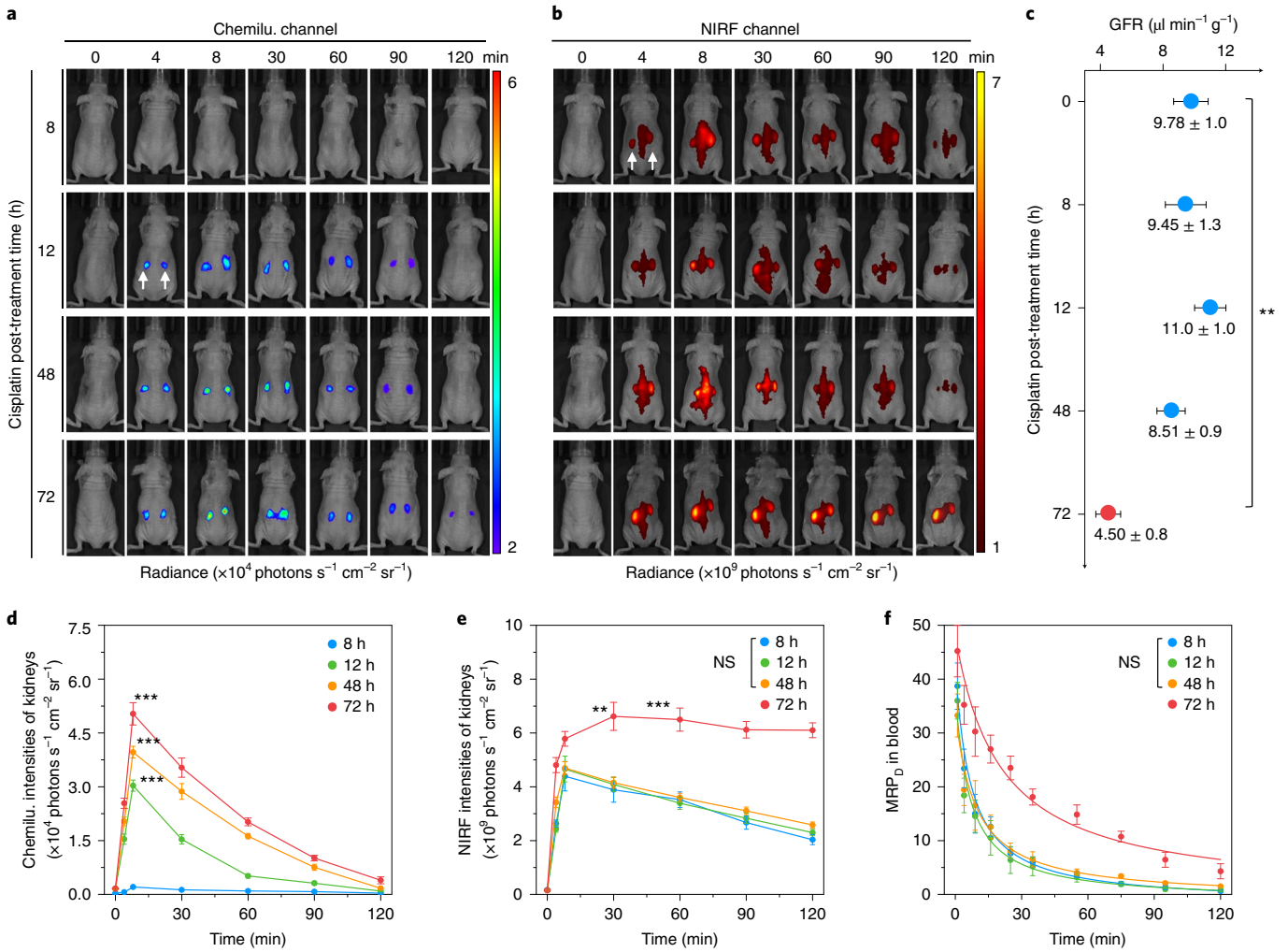

Fig. 5 | Real-time in vivo dual-channel imaging of cisplatin-induced AKI. a,**b**, Representative chemiluminescence (**a**) and NIRF (**b**) images of living mice with i.v. injection of MRP_D after treatment with cisplatin (20 mg kg^{-1} body weight) for 8, 12, 48 or 72 h. The experiments were repeated independently three times with similar results. **c**, GFR of living mice at $t = 8$, 12, 48 or 72 h post-treatment with cisplatin, or saline, measured by the standard fluorescein isothiocyanate (FITC)–inulin method. The data are the mean ± s.d.; $n = 3$ independent mice; two-tailed Student's t-test; pre-treatment versus 8, 12, 48 h post-treatment groups, not significant; pre-treatment versus 72 h post-treatment group, $^{**}P < 0.01$. **d**,**e**, The dynamic chemiluminescence (**d**) and NIRF (**e**) intensities of kidneys as a function of time post-injection of MRP_D in living mice after treatment with cisplatin for 8, 12, 48 or 72 h. The data are the mean ± s.d.; $n = 3$ independent mice; two-tailed Student's t-test; 8 h post-treatment versus 12, 48 or 72 h post-treatment groups, NS: not significant, $^{**}P < 0.01$, $^{***}P < 0.001$. **f**, Blood concentration (%ID g^{-1}) decay of MRP_D in living mice at $t = 8$, 12, 48 or 72 h post-treatment with cisplatin. The data are the mean ± s.d.; $n = 3$ independent mice; two-tailed Student's t-test; 8 h post-treatment versus 12 or 48 h post-treatment groups, NS: not significant.

To gain insight into the origin of probe retention in the kidneys, the pharmacokinetics of MRP_D (Fig. 5f) and the glomerular filtration rate (GFR; Fig. 5c) were measured in the mice at different time points post-treatment with cisplatin. The blood elimination half-lives ($t_{1/2\beta}$) of MRP_D in the mice after cisplatin treatment for 8, 12 and 48 h were similar (14.3 min), but it prolonged to 34.7 min for 72 h. This was ascribed to the significantly decreased GFR from 9.78 before treatment to 4.50 μl min^{-1} g^{-1} body weight at 72 h post-treatment. Thus, these data further proved that the probe retention was caused by declined glomerular filtration capability under nephrotoxic expose, consistent with the histological data showing renal tubular damage (Supplementary Fig. 13). Moreover, the fact that the chemiluminescent signal of MRP_D was detected at 12 h before the decrease in GFR indicated the ability of MRP_D for early detection of drug-induced AKI. Similar trends of dual-channel imaging results and GFR changes were observed for MRP_D in the mouse model of gentamicin- or diatrizoate-induced AKI (Supplementary Figs. 19–21).

In vitro diagnosis

To evaluate the translational potential of MRPs, drug-induced AKI was detected in urine and compared with existing assays. Two methods were used for MRP-based urinalysis (Fig. 6a): direct NIRF measurement of excreted probes in urine after their i.v. injection into drug-treated mice (online urinalysis); and collection of urine samples from drug-treated mice followed by probe incubation and optical measurement (offline urinalysis). In the online urinalysis (Fig. 6b–d and Supplementary Figs. 22 and 23), the first statistically significant NIRF enhancement was respectively observed at 12 (2.0-fold), 36 (2.3-fold) and 8 h (2.1-fold) post-treatment with cisplatin, gentamicin and diatrizoate for excreted MRP1, 16 (2.3-fold), 48 (2.3-fold) and 16 h (2.4-fold) for MRP2, and 48 (2.6-fold), 144 (2.8-fold) and 24 h (1.9-fold) for MRP3. Moreover, the NIRF signal continued increasing after these time points. The signal evolution behaviours of MRPs coincided with the real-time NIRF imaging data, as the excreted MRPs were activated in the renal clearance

pathway. In the offline urinalysis (Fig. 6e–g and Supplementary Fig. 23), only MRP2 showed statistically significant NIRF enhancement after incubation in urine because $O_2^{\bullet-}$ has a short half-life (<5 s)[34], and caspase-3 is an intracellular enzyme that is excreted less in urine[35]. The earliest time points for MRP2 to detect the upregulation of NAG in the offline urinalysis were 24 (2.7-fold), 72 (2.1-fold) and 24 (2.7-fold) for cisplatin-, gentamicin- and diatrizoate-treated mice, respectively. These were slightly later (8–24 h) than those in the online urinalysis, probably due to the diluted concentration of NAG in the urine relative to that in the kidneys.

Commercial assays were used to measure sCr, BUN and cystatin C in blood as well as NGAL, clusterin, KIM-1, osteopontin, β2-microglobulin and trefoil factor-3 in urine. The sCr and BUN had a statistically significant increase at 72 (2.4, 2.0-fold), 144 (2.9, 2.4-fold) and 24 h (1.8, 2.0-fold) after treatment with cisplatin, gentamicin and diatrizoate, respectively (Fig. 6h–j). At these time points, the GFRs were decreased by ~50% (Supplementary Fig. 21). The serum cystatin C behaved similarly in the gentamicin and diatrizoate models but increased earlier at 48 h (2.0-fold) in the cisplatin model. Among the tested urinary biomarkers, KIM-1 and clusterin were most sensitive, showing their first statistically significant increases at 24 (1.9, 4.1-fold), 72 (2.2, 3.5-fold) and 24 h (3.7, 3.0-fold) after treatment with cisplatin, gentamicin and diatrizoate, respectively. However, the first statistically significant changes of NGAL and trefoil factor-3 were observed at 48 (2.7, 0.4-fold), 96 (2.0, 0.3-fold) and 24 h (2.3, 0.5-fold) post-treatment with cisplatin, gentamicin and diatrizoate, respectively. The statistically significant changes of osteopontin and β2-microglobulin after treatment with cisplatin, gentamicin and diatrizoate occurred even later: 72 (2.3-fold) (cisplatin), 144 (2.3-fold) (gentamicin) and 24 h (2.3-fold) (diatrizoate) for osteopontin, and 72 (3.9-fold) (cisplatin), 144 (3.2-fold) (gentamicin) and 48 h (3.6-fold) (diatrizoate) for β2-microglobulin.

Comparison of the urinal/plasma analysis data (Fig. 6k–m) revealed that the MRP1/MRP2-based online urinalysis of upregulated $O_2^{\bullet-}$/NAG was most sensitive to detect drug-induced AKI. The first statistically significant change of the MRP1/MRP2-based online urinalysis detected drug-induced AKI at least 12/8 (cisplatin), 36/24 (gentamicin) and 16/8 h (diatrizoate) earlier than both MRP2-based offline urinalysis and KIM-1- or clusterin-based urinalysis, and at least 36/32 (cisplatin), 60/48 (gentamicin) and 16/8 h (diatrizoate) earlier than the clinical methods and other tested preclinical assays.

Summary and outlook

The fundamental limitation in molecular imaging of AKI is a lack of molecular probes that simultaneously possess high renal clearance efficiency and activatable signals specific to early AKI biomarkers. On substitution of HPβCD, MRPs1–3, MRP_D and CCD had renal clearance efficiencies (>97% ID at 24 h post-injection) higher than all existing imaging agents regardless of their imaging modalities and compositions (Supplementary Table 4) such as gold nanoclusters (52% ID)[36], quantum dots (75% ID)[37], silica Cornell dots (73%)[38] and zwitterionic fluorophores (86% ID)[39]. Even in drug-treated mice, the renal clearance efficiencies of MRPs were >82% ID at 24 h post-injection (Supplementary Fig. 24). The nearly complete renal clearance allowed the HPβCD-substituted fluorophore (CCD) to clearly delineate both kidneys of living mice through the entire imaging course (Supplementary Fig. 7a); in contrast, PEG-substituted CP2 and CP5 and other reported fluorophores failed to do so due to the signal interference from the fluorophore uptake by other organs[40].

The high sensing specificity and ideal in vivo stability of MRPs1–3 in association with their nearly identical pharmacokinetics permitted longitudinal imaging of multiple biomarkers ($O_2^{\bullet-}$, NAG and caspase-3) in the kidneys of drug-treated living mice. The real-time imaging results from three representative nephrotoxic drugs (cisplatin, gentamicin and diatrizoate) consistently showed that oxidative stress, lysosomal damage and cellular apoptosis were prodromal molecular events occurring sequentially after nephrotoxic exposure. In comparison with the fluorescent turn-on probe (MRP1), MRP_D sensed the upregulation of $O_2^{\bullet-}$ at the same time point but had a higher signal- to- background ratio (SBR; up 21-fold) due to minimized tissue autofluorescence in chemiluminescence imaging (Supplementary Fig. 25). Moreover, MRP_D is the first probe of its kind with always-on fluorescence but biomarker-activated chemiluminescence[19,41,42]. Such an uncoordinated and intrinsically independent dual-channel imaging capability enabled MRP_D to non-invasively validate that the chemiluminescence signal was activated by upregulated $O_2^{\bullet-}$ before the retention-caused enhancement of NIRF signals (Fig. 5).

Comparison of the detection timelines of MRPs with the changes in GFR after nephrotoxic exposure (Fig. 6k–m) directly proved that MRPs1 and 2 and MRP_D detected AKI before a decrease in glomerular filtration. In particular, MRPs1–3 sequentially detected upregulated $O_2^{\bullet-}$, NAG and caspase-3 at 12, 16 and 48 h post-treatment in the cisplatin model of AKI. These time points were at least 36 h earlier than those for other real-time imaging methods based on the bioluminescent NGAL (168 h)[43] or transcription factor nuclear factor erythroid 2-related factor 2 (Nrf2) (a major regulator responding to oxidative stress) (48 h) reporter genes[44] as well as the retention-based magnetic resonance imaging, contrast-enhanced computed tomography and single-photon emission computed tomography contrast agents detecting the changes in glomerular filtration (>72 h)[14] in the mouse model with the same drug dosage (20 mg kg^{-1}) (Supplementary Tables 5 and 6). Such early detection capability of MRPs was also validated in other animal settings with the variation in drug dosages (Supplementary Figs. 26–28), mouse strains (Supplementary Figs. 29 and 30) and mouse ages (Supplementary Fig. 31).

Fig. 6 | In vitro diagnosis of drug-induced AKI in living mice. a, A schematic illustration of the workflows for optical urinalysis of drug-induced AKI in living mice. Online urinalysis: fluorescence readouts of excreted MRPs1–3 in the urine from drug-treated living mice after i.v. injection of MRPs1–3 at different time points post-treatment with drug. Offline urinalysis: fluorescence readouts of MRPs1–3 after incubation with urine samples collected from drug-treated living mice at different time points post-treatment with drug. The commercial assays were used to measure Cr, BUN and Cyst C in the blood as well as NGAL, TFF3, OPN, β2-microglobulin, KIM-1 and clusterin in the urine samples collected from drug-treated living mice at different time points post-treatment with drug. **b**–**d**, Fluorescence enhancement of excreted MRPs1–3 in the urine from drug-treated living mice after i.v. injection of MRPs1–3 at different time points post-treatment with drug. **e**–**g**, Fluorescence enhancement of MRPs1–3 after incubation with the urine samples collected from drug-treated living mice at different time points post-treatment with drug. The data are the mean ± s.d.; $n = 9$ independent experiments for **b**–**d** and **e**–**g**; two-tailed Student's *t*-test; pre-treatment versus post-treatment groups, $^{**}P < 0.01$, $^{***}P < 0.001$. **h**–**j**, Fold change in urinary and serum biomarkers at different time points post-treatment with drug. The data are the mean ± s.d.; $n = 5$ independent experiments for Cr, BUN, Cyst C, NGAL and KIM-1; $n = 6$ independent experiments for TFF3, OPN, β2-microglobulin and clusterin; two-tailed Student's *t*-test; pre-treatment versus post-treatment groups, $^{*}P < 0.05$, $^{**}P < 0.01$, $^{***}P < 0.001$. **k**–**m**, A timeline comparing MRPs (online and offline urinalysis) to the clinical methods and Food and Drug Administration-qualified urinary biomarkers for detection of drug-induced AKI. The data are the mean ± s.d. $n = 5$ independent experiments for Cr, BUN, Cyst C, NGAL and KIM-1; $n = 6$ independent experiments for TFF3, OPN, β2-microglobulin and clusterin.

Thus, the MRPs are by far the most sensitive probes that detect AKI at the incipient stage, which is imperative for timely initiation of renoprotective intervention to deter transition into more severe complications and aid in recovery from AKI for hospitalized patients. Moreover, MRPs could even potentially detect drug-induced AKI on the backdrop of diabetes-related chronic kidney disease (Supplementary Figs. 32 and 33), making them highly competent for drug development.

MRPs1–3 are promising for clinical diagnosis, because they are non-toxic and rapidly cleared renally. Although optical imaging has a relatively shallow imaging depth and thus is less suitable for real-time imaging of kidneys in patients, MRPs1–3 can act as

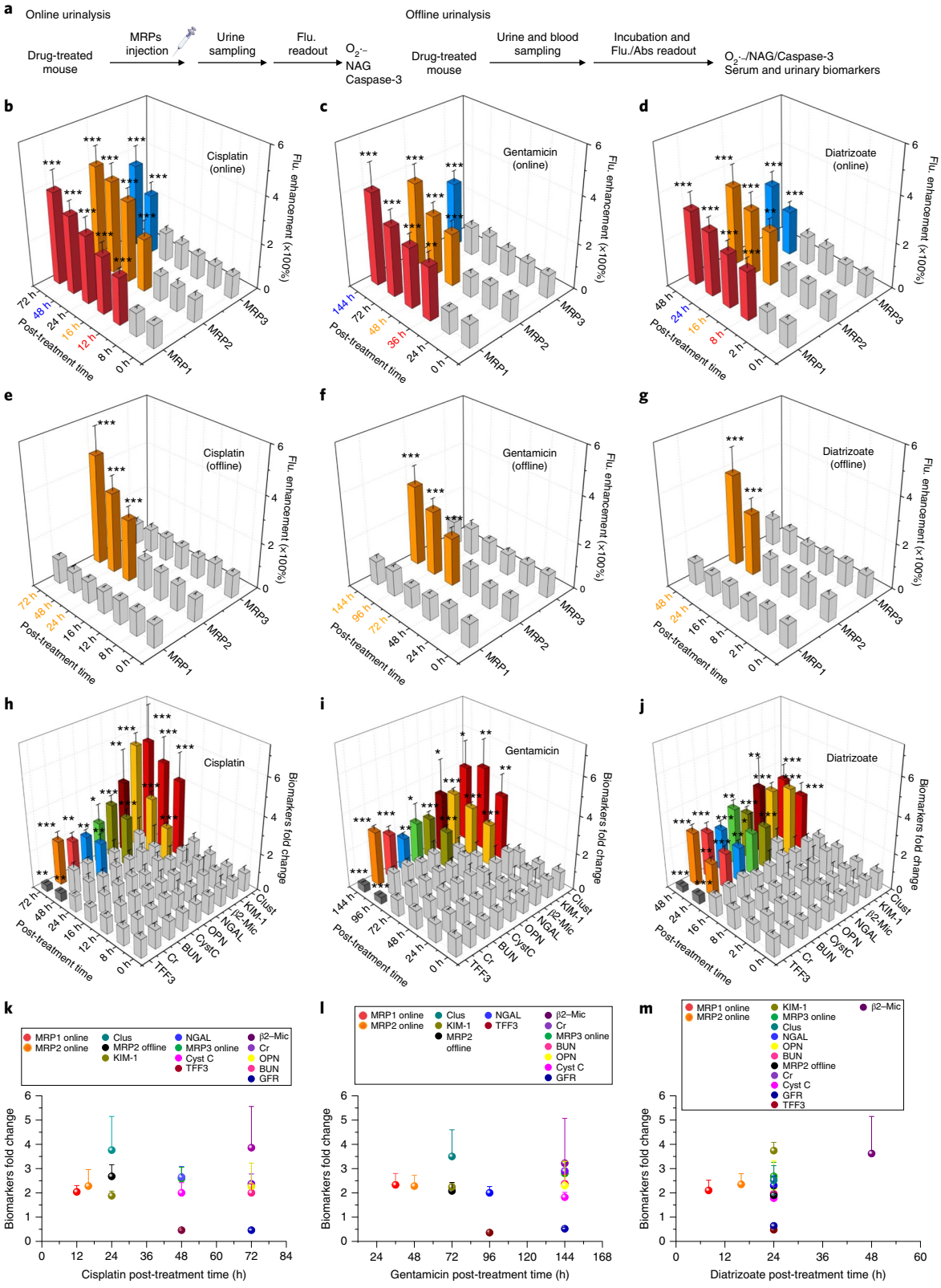

exogenous tracers for optical urinalysis. In the MRP-based online urinalysis, the signals of the excreted probes were detected as early as in the real-time imaging approach (Fig. 6b–d versus Fig. 3b–d)—these were again 16 to 108 h earlier than the 50% decrease in GFR depending on the drugs. In addition, the presence of urinary NAG allowed MRP2 to be valid for offline urinalysis simply by pre-incubation with mouse urine before optical analysis. Despite the slightly delayed detection time points relative to the online urinalysis, MRP2-based offline urinalysis still outperformed most of the tested clinical assays and identified AKI 24–72 h earlier than the NAGL, Cyst C and β2-microglobulin assay (three assays better than sCr/BUN)[24] in a cisplatin- or gentamicin-induced AKI mouse model (Fig. 6k). Moreover, NAG has a molecular weight (140 kDa) larger than the glomerular filtration cutoff (50 kDa), ensuring that plasma NAG produced from other organs cannot be filtered through the glomerulus and excreted into the urine[45]. Thereby, MRP2-based offline urinalysis should be specific to the AKI-induced renal NAG. Indeed, no signal enhancement was detected for MRP2 after incubation with urine from mice with local inflammation (Supplementary Fig. 34) or liver injury (Supplementary Fig. 35).

In summary, we synthesized renal-clearable molecular probes for real-time optical imaging of sequential prodromal molecular events in the kidney of living mice undergoing nephrotoxic exposure. Such probes represent a type of imaging agent that almost completely goes through renal clearance, specifically reacts with the targeted biomarkers in kidneys, and spontaneously activates its optical signals to report abnormal upregulation at the incipient stage of drug-induced AKI before the decrease in GFR. The ability of MRPs to be used as urinalysis tracers to detect drug-induced AKI earlier than current assays further underlines their potential in clinical translation. Our work thus opens up a molecular imaging approach that not only permits mechanistic investigation of nephrotoxicity and high-throughput drug screening in living animals, but also facilitates validation and translation of new biomarkers for diagnosis of kidney injury.

Online content

Any methods, additional references, Nature Research reporting summaries, source data, statements of code and data availability and associated accession codes are available at https://doi.org/10.1038/s41563-019-0378-4.

Received: 26 September 2018; Accepted: 16 April 2019;
Published online: 27 May 2019

References

1. Chawla, L. S., Eggers, P. W., Star, R. A. & Kimmel, P. L. Acute kidney injury and chronic kidney disease as interconnected syndromes. *N. Engl. J. Med.* **371**, 58–66 (2014).
2. Abuelo, J. G. Normotensive ischemic acute renal failure. *N. Engl. J. Med.* **357**, 797–805 (2007).
3. Alobaidi, R., Basu, R. K., Goldstein, S. L. & Bagshaw, S. M. Sepsis-associated acute kidney injury. *Semin. Nephrol.* **35**, 2–11 (2015).
4. Kellum, J. A. & Prowle, J. R. Paradigms of acute kidney injury in the intensive care setting. *Nat. Rev. Nephrol.* **14**, 217–230 (2018).
5. Soo, J. Y. C., Jansen, J., Masereeuw, R. & Little, M. H. Advances in predictive in vitro models of drug-induced nephrotoxicity. *Nat. Rev. Nephrol.* **14**, 378–393 (2018).
6. Perazella, M. A. & Coca, S. G. Three feasible strategies to minimize kidney injury in 'incipient AKI'. *Nat. Rev. Nephrol.* **9**, 484–490 (2013).
7. Darmon, M. et al. Diagnostic work-up and specific causes of acute kidney injury. *Intensive Care Med.* **43**, 829–840 (2017).
8. Wang, X. et al. Validation of creatinine-based estimates of GFR when evaluating risk factors in longitudinal studies of kidney disease. *J. Am. Soc. Nephrol.* **17**, 2900–2909 (2006).
9. Lameire, N. H. et al. Acute kidney injury: an increasing global concern. *Lancet* **382**, 170–179 (2013).
10. Willmann, J. K., Van Bruggen, N., Dinkelborg, L. M. & Gambhir, S. S. Molecular imaging in drug development. *Nat. Rev. Drug Discov.* **7**, 591–607 (2008).
11. Miao, Q. et al. Molecular afterglow imaging with bright, biodegradable polymer nanoparticles. *Nat. Biotechnol.* **35**, 1102–1110 (2017).
12. Lovell, J. F. et al. Porphysome nanovesicles generated by porphyrin bilayers for use as multimodal biophotonic contrast agents. *Nat. Mater.* **10**, 324–332 (2011).
13. Ntziachristos, V., Ripoll, J., Wang, L. V. & Weissleder, R. Looking and listening to light: the evolution of whole-body photonic imaging. *Nat. Biotechnol.* **23**, 313–320 (2005).
14. Grenier, N., Merville, P. & Combe, C. Radiologic imaging of the renal parenchyma structure and function. *Nat. Rev. Nephrol.* **12**, 348–359 (2016).
15. Hong, G., Antaris, A. L. & Dai, H. Near-infrared fluorophores for biomedical imaging. *Nat. Biomed. Eng.* **1**, 0010 (2017).
16. So, M. K., Xu, C., Loening, A. M., Gambhir, S. S. & Rao, J. Self-illuminating quantum dot conjugates for in vivo imaging. *Nat. Biotechnol.* **24**, 339–343 (2006).
17. Smith, A. M., Mancini, M. C. & Nie, S. Bioimaging: second window for in vivo imaging. *Nat. Nanotechnol.* **4**, 710–711 (2009).
18. Ning, X. et al. Maltodextrin-based imaging probes detect bacteria in vivo with high sensitivity and specificity. *Nat. Mater.* **10**, 602–607 (2011).
19. Chan, J., Dodani, S. C. & Chang, C. J. Reaction-based small-molecule fluorescent probes for chemoselective bioimaging. *Nat. Chem.* **4**, 973–984 (2012).
20. Park, S. M., Aalipour, A., Vermesh, O., Yu, J. H. & Gambhir, S. S. Towards clinically translatable in vivo nanodiagnostics. *Nat. Rev. Mater.* **2**, 17014 (2017).
21. Vaidya, V. S. et al. Kidney injury molecule-1 outperforms traditional biomarkers of kidney injury in preclinical biomarker qualification studies. *Nat. Biotechnol.* **28**, 478–485 (2010).
22. Yu, Y. et al. Urinary biomarkers trefoil factor 3 and albumin enable early detection of kidney tubular injury. *Nat. Biotechnol.* **28**, 470–477 (2010).
23. Ozer, J. S. et al. A panel of urinary biomarkers to monitor reversibility of renal injury and a serum marker with improved potential to assess renal function. *Nat. Biotechnol.* **28**, 486–494 (2010).
24. Dieterle, F. et al. Urinary clusterin, cystatin C, β2-microglobulin and total protein as markers to detect drug-induced kidney injury. *Nat. Biotechnol.* **28**, 463–469 (2010).
25. Sureshbabu, A., Ryter, S. W. & Choi, M. E. Oxidative stress and autophagy: crucial modulators of kidney injury. *Redox Biol.* **4**, 208–214 (2015).
26. Ware, L. B., Fessel, J. P., May, A. K. & Roberts, L. J. 2nd Plasma biomarkers of oxidant stress and development of organ failure in severe sepsis. *Shock* **36**, 12–17 (2011).
27. Naud, J. F. & Leblanc, M. Biomarkers in acute kidney injury. *Kidney Int.* **3**, 115–125 (2008).
28. Miao, Q. et al. Near-infrared fluorescent molecular probe for sensitive imaging of keloid. *Angew. Chem. Int. Ed.* **57**, 1256–1260 (2018).
29. Hananya, N., Eldar Boock, A., Bauer, C. R., Satchi Fainaro, R. & Shabat, D. Remarkable enhancement of chemiluminescent signal by dioxetane-fluorophore conjugates: turn-on chemiluminescence probes with color modulation for sensing and imaging. *J. Am. Chem. Soc.* **138**, 13438–13446 (2016).
30. Galgamuwa, R. et al. Dichloroacetate prevents cisplatin-induced nephrotoxicity without compromising cisplatin anticancer properties. *J. Am. Soc. Nephrol.* **27**, 3331–3344 (2016).
31. Otunctemur, A. et al. Protective effect of hydrogen sulfide on gentamicin-induced renal injury. *Ren. Fail.* **36**, 925–931 (2014).
32. Erley, C. M. et al. Prevention of radiocontrast-induced nephropathy by adenosine antagonists in rats with chronic nitric oxide deficiency. *J. Am. Soc. Nephrol.* **8**, 1125–1132 (1997).
33. Basile, D. P., Anderson, M. D. & Sutton, T. A. Pathophysiology of acute kidney injury. *Compr. Physiol.* **2**, 1303–1353 (2012).
34. Hayyan, M., Hashim, M. A. & AlNashef, I. M. Superoxide ion: generation and chemical implications. *Chem. Rev.* **116**, 3029–3085 (2016).
35. Zhivotovsky, B., Samali, A., Gahm, A. & Orrenius, S. Caspases: their intracellular localization and translocation during apoptosis. *Cell Death Differ* **6**, 644–651 (1999).
36. Du, B. et al. Glomerular barrier behaves as an atomically precise bandpass filter in a sub-nanometre regime. *Nat. Nanotechnol.* **12**, 1096–1102 (2017).
37. Choi, H. S. et al. Renal clearance of quantum dots. *Nat. Biotechnol.* **25**, 1165–1170 (2007).
38. Burns, A. A. et al. Fluorescent silica nanoparticles with efficient urinary excretion for nanomedicine. *Nano Lett.* **9**, 442–448 (2009).
39. Owens, E. A., Henary, M., El Fakhri, G. & Choi, H. S. Tissue-specific near-infrared fluorescence imaging. *Acc. Chem. Res.* **49**, 1731–1740 (2016).
40. Antaris, A. L. et al. A small-molecule dye for NIR-II imaging. *Nat. Mater.* **15**, 235–242 (2016).
41. Dickinson, B. C. & Chang, C. J. Chemistry and biology of reactive oxygen species in signaling or stress responses. *Nat. Chem. Biol.* **7**, 504–511 (2011).
42. Shuhendler, A. J., Pu, K., Cui, L., Uetrecht, J. P. & Rao, J. Real-time imaging of oxidative and nitrosative stress in the liver of live animals for drug-toxicity testing. *Nat. Biotechnol.* **32**, 373–380 (2014).

43. Paragas, N. et al. The Ngal reporter mouse detects the response of the kidney to injury in real time. *Nat. Med.* **17**, 216–222 (2011).
44. Forootan, S. S. et al. Real-time in vivo imaging reveals localised Nrf2 stress responses associated with direct and metabolism-dependent drug toxicity. *Sci. Rep.* **7**, 16084 (2017).
45. Asami, T., Soichiro, O., Kasahara, T. & Uchiyama, M. Asymptomatic primary hyper-*N*-acetyl-beta-D-glucosaminidaseuria: a new clinical entity? *Pediatr. Nephrol.* **17**, 560–565 (2002).

Acknowledgements

K.P. thanks Nanyang Technological University (startup grant: M4081627) and Singapore Ministry of Education, Academic Research Fund Tier 1 (2017–T1–002–134–RG147/17) and Academic Research Fund Tier 2 (MOE2016–T2–1–098) for the financial support.

Author contributions

K.P. and J.H. conceived and designed the study. J.H. and Q.M. performed the probe synthesis experiments. J.H. performed the in vivo experiments. J.H, J.L. and Y.L. performed the histology experiments. K.P. and J.H. contributed to the analysis and interpretation of the results and the writing of the manuscript.

Competing interests

The authors declare no competing interests.

Additional information

Supplementary information is available for this paper at https://doi.org/10.1038/s41563-019-0378-4.

Reprints and permissions information is available at www.nature.com/reprints.

Correspondence and requests for materials should be addressed to K.P.

Publisher's note: Springer Nature remains neutral with regard to jurisdictional claims in published maps and institutional affiliations.

© The Author(s), under exclusive licence to Springer Nature Limited 2019

Methods

Chemicals. All chemicals were purchased from Sigma-Aldrich or Tokyo Chemical Industry unless otherwise stated. Cisplatin, gentamicin, diatrizoate, α-naphthyl isothiocyanate (ANIT) and lipopolysaccharides (LPS, from *Escherichia coli* 0111:B4) were obtained from Sigma-Aldrich. NAG, plasmin, β-Gal, nitroreductase and FAPα were purchased from Sigma-Aldrich. AAP, furin and recombinant human caspase-3 were purchased from R&D Systems. The creatinine assay kit, urea assay kit and mouse cystatin C ELISA kit were purchased from Sigma-Aldrich, BioAssay Systems and RayBiotech, respectively. The mouse NGAL, osteopontin, KIM-1, TFF3 and clusterin ELISA kit were purchased from R&D Systems. Cleaved-caspase-3 antibody (9661L) was purchased from Cell Signaling Technology. The mouse beta2-microglobulin ELISA kit, anti-CD31 antibody (ab28364), anti-CD11b antibody (ab133357) and Alexa Fluor 488-conjugated goat anti-rabbit IgG H&L (ab150077) were purchased from Abcam. Ultrapure water was supplied by Milli-Q Plus System (Millipore).

Materials characterization. Silica gel (Silicycle, 230–400 mesh) was used for column chromatography. Thin-layer chromatography (TLC) was conducted on silica gel glass plates coated with the fluorescent indicator F-254 (Merck). Absorption and fluorescence spectra were recorded on a UV-2450 spectrophotometer (Shimadzu) and a Fluorolog 3-TCSPC spectrofluorometer (Horiba Jobin Yvon) using quartz cuvettes, respectively. Chemiluminescence was recorded on a spectramax i3x (Molecular Devices) or Luminometer (Promega). HPLC analyses and purification were performed on an Agilent 1260 system using acetonitrile (CH_3CN)/water (H_2O) as the eluent (Supplementary Table 7). ^{1}H NMR spectra were conducted with a Bruker 300 MHz NMR instrument. Electrospray ionization-mass spectrometry (ESI-MS) spectra were conducted with a Thermo Finnigan Polaris Q quadrupole ion trap mass spectrometer (ThermoFisher Corporation) equipped with a standard ESI source. MALDI time-of-flight (TOF) analyses were conducted on a Bruker ultraflex TOF/TOF instrument. The pH values were measured with a digital pH meter (SevenCompact S220). Tissues were cut into sections using a cryostat (Leica). The tissue sections were examined on a Nikon ECLIPSE 80i microscope (Nikon Instruments). Confocal microscopy images of tissue sections were acquired on an LSM800 confocal laser scanning microscope (Carl Zeiss). Fluorescence and chemiluminescence imaging were performed on the IVIS spectrum imaging system (PerkinElmer), and the Living Image 4.3 software was used to analyse the region of interest. In silico calculation of the partition coefficients (log[*D*]) was calculated using Marvin and JChem calculator plug-ins (ChemAxon). Blood samples were collected using heparinized capillary tubes (Paul Marienfeld). Urine samples were collected with metabolic cages (Lab Products).

Synthesis of BrGlcNAc. AcGlcNAc (0.78 g, 2.0 mmol) was dissolved in anhydrous dichloromethane (CH_2Cl_2) (8 ml), followed by addition of hydrogen bromide (33% in acetic acid, 5 ml). After the reaction mixture was stirred in an ice bath for 8 h, it was poured into cold H_2O and extracted by CH_2Cl_2. The organic layer was washed with saturated sodium hydrogen carbonate ($NaHCO_3$) aqueous solution, dried over anhydrous sodium sulfate (Na_2SO_4) and concentrated under a vacuum to afford BrGlcNAc (0.62 g, 75%) as a white crystalline solid. TLC (silica gel, ethyl acetate (EA)/petroleum ether (PE) = 1/3), R_f = 0.4. ^{1}H NMR (300 MHz, $CDCl_3$): δ 2.00 (s, 3H), 2.07 (s, 6H), 2.11 (s, 3H), 4.11 (d, *J* = 3, 1H), 4.16 (t, 1H), 4.24 (t, 1H), 5.30 (m, 2H), 5.82 (d, *J* = 9, 1H), 6.52 (d, *J* = 6, 1H). ESI-MS (*m*/*z*): calcd: 409.04, found [M-Br]: 330.1.

Synthesis of Br-Ph-DVED. Ac-DEVD (0.69 g, 1.0 mmol) was dissolved in tetrahydrofuran (THF) (20 ml), followed by addition of (4-aminophenyl) methanol (0.49 g, 4.0 mmol) and *N*-ethoxycarbonyl-2-ethoxy-1, 2-dihydroquinoline (0.99 g, 4.0 mmol). The mixture was stirred at 25 °C for 12 h before conducting concentration under a vacuum. The residue was washed with H_2O, extracted with CH_2Cl_2, and concentrated under a vacuum followed by HPLC purification to give compound Ph-DVED (0.63 g, 80%). Ph-DVED (0.40 g, 0.5 mmol) was dissolved in THF (25 ml), followed by addition of phosphorus tribromide (PBr_3) (0.27 g, 1.0 mmol). The reaction mixture was stirred at 25 °C for 12 h and then quenched with H_2O, followed by extraction with CH_2Cl_2 and concentrated under a vacuum. Purification of the residue by preparative HPLC gave Br-Ph-DVED (0.32 g, 76% yield). ^{1}H NMR (300 MHz, $CDCl_3$): δ 0.95 (s, 6H), 1.43 (s, 27H), 2.08 (s, 3H), 2.22 (m, 3H), 2.53 (m, 3H), 2.85 (m, 4H), 4.35 (m, 3H), 4.76 (s, 3H), 7.11 (d, *J* = 6 Hz, 1H), 7.31 (d, *J* = 3 Hz, 1H), 7.52 (d, *J* = 3 Hz, 1H), 7.92 (s, 1H). ESI-MS (*m*/*z*): calcd: 853.35, found [M-Br]: 774.21.

Synthesis of propynyl-HPβCD. To a solution of HPβCD (3.08 g, 2.0 mmol) and tetra-*tert*-butylammonium iodide (0.16 g, 0.44 mmol) in anhydrous dimethylformamide (DMF) (15 ml) was added a suspension of sodium hydride (NaH) (0.80 g, 20 mmol, 60% dispersion in mineral oil) in anhydrous DMF (25 ml) in an ice bath. After stirring for 30 min in the ice bath, a solution of propargyl bromide (0.30 g, 3.0 mmol) in anhydrous DMF (1 ml) was added. The reaction mixture was stirred at 25 °C for an additional 24 h before it was concentrated under a vacuum. Purification of the residue by silica gel column chromatography gave propynyl-HPβCD (3.02 g, 94%) as a yellowish solid after freeze drying. ^{1}H NMR (300 MHz, D_2O): δ 1.14 (d, *J* = 6, 17H), 2.72 (s, 1H), 3.25–4.25 (m, 64H), 5.08–5.25 (m, 7H). MALDI-TOF MS found: 1,400–1,800.

Synthesis of CMe and CyOH. CMe and CyOH were synthesized according to our previous study[28]. ^{1}H NMR of CMe (300 MHz, $CDCl_3$): δ 1.65 (s, 6H), 1.88 (m, 2H), 2.63 (m, 4H), 3.33 (s, 3H), 5.54 (d, *J* = 15 Hz, 1H), 6.55 (s, 1H), 6.76 (m, 2H), 7.04–7.24 (m, 3H), 7.29 (m, 2H), 8.03 (t, 1H). ESI-MS of CMe (*m*/*z*): calcd: 384.19, found: 384.40. ^{1}H NMR of CyOH (300 MHz, $CDCl_3$): δ 1.76 (s, 6H), 1.96 (m, 8H), 2.71 (t, 2H), 3.47 (t, 2H), 4.21 (d, *J* = 6 Hz, 2H), 5.30 (s, 1H), 6.11 (d, *J* = 15 Hz, 1H), 7.17 (m, 3H), 7.44 (m, 4H), 7.71 (m, 1H), 8.50 (d, *J* = 15 Hz, 1H). ESI-MS of CyOH (*m*/*z*): calcd: 467.2, found: 467.2.

Synthesis of MRP1. A mixture of CyOH (46.70 mg, 0.1 mmol), diphenylphosphinyl chloride (46.0 µl, 0.24 mmol) and triethylamine (56.0 µl, 0.4 mmol) in CH_2Cl_2 (10 ml) was stirred at 25 °C. After 15 min, the reaction mixture was concentrated under a vacuum to give compound CS as a blue solid. ESI-MS (*m*/*z*): calcd: 667.2, found: 667.3. Compound CS (83 mg, 0.125 mmol) was dissolved in H_2O (1 ml) and stirred at 25 °C for 10 min. To above solution, propynyl-HPβCD (0.20 g, 0.125 mmol), sodium ascorbate (4.60 mg, 0.022 mmol) and cupric sulfate ($CuSO_4{\cdot}5H_2O$) (7.50 mg, 0.03 mmol) in dimethylsulfoxide (DMSO)/H_2O (2 ml/2 ml) were added. The mixture was stirred at 25 °C under a nitrogen atmosphere in the dark for 5 h, and then precipitated in acetone. Further purification by preparative HPLC gave MRP1 (0.20 g, 80% yield) as a blue solid. ^{1}H NMR (300 MHz, D_2O): δ 1.14 (m, 18H), 1.73–2.12 (m, 15H), 2.45 (m, 2H), 2.94 (m, 3H), 3.25–4.25 (m, 83H), 4.28 (m, 2H), 5.07–5.31 (m, 13H), 5.58 (m, 2H), 6.04 (s, 1H), 6.85–8.47 (m, 16H). MALDI-TOF MS found: 1,600–2,300.

Synthesis of MRP2. A mixture of CyOH (23.40 mg, 0.05 mmol) and caesium carbonate (Ce_2CO_3) (0.07 g, 0.2 mmol) in anhydrous CH_2Cl_2 (3 ml) was stirred at 25 °C under a nitrogen atmosphere for 15 min. To the above solution, BrGlcNAc (0.08 g, 0.2 mmol) was added and stirred at 25 °C for an additional 16 h. Then the reaction was poured into H_2O, extracted by CH_2Cl_2 and concentrated under a vacuum to yield the crude product. To a solution of the above crude product (26.40 mg, 0.033 mmol) in methanol (4 ml) was added sodium methoxide (CH_3ONa) solution (0.07 g, 0.33 mmol, 25% in methanol). The reaction mixture was stirred at 25 °C for 10 min before conducting concentration under a vacuum. The product was purified by silica gel column chromatography to afford compound CN as a blue solid. ^{1}H NMR (300 MHz, CD_3OD): δ 1.84 (d, 3H), 1.91 (s, 6H), 2.00 (m, 4H), 2.03 (s, 2H), 2.18 (m, 2H), 2.76 (m, 2H), 3.45 (m, 2H), 3.60–4.10 (m, 6H), 4.41 (s, 2H), 4.61 (d, *J* = 9 Hz, 1H), 5.11 (d, *J* = 3 Hz, 1H), 5.34 (t, 1H), 6.56 (d, *J* = 15 Hz, 1H), 7.03 (d, *J* = 3 Hz, 1H), 7.20 (s, 1H), 7.40–7.60 (m, 5H), 8.79 (d, *J* = 15 Hz, 1H). ESI-MS (*m*/*z*): calcd: 670.3, found: 670.3. Compound CN (23 mg, 0.033 mmol) and propynyl-HPβCD (53 mg, 0.033 mmol) were dissolved in DMSO/H_2O (2 ml/2 ml), followed by addition of a solution of sodium ascorbate (2.0 mg, 0.01 mmol) and $CuSO_4{\cdot}5H_2O$ (2.5 mg, 0.01 mmol) in H_2O. After the reaction mixture was stirred at 25 °C under a nitrogen atmosphere in the dark for 5 h, precipitation was conducted in acetone. Further purification by preparative HPLC gave MRP2 (58 mg, 85% yield) as a blue solid. ^{1}H NMR (300 MHz, D_2O): δ 1.20 (m, 18H), 1.80–2.13 (m, 15H), 2.70 (m, 3H), 3.00 (m, 3H), 3.25–4.25 (m, 70H), 4.32 (m, 3H), 5.15–5.31 (m, 9H), 5.60–5.75 (m, 2H), 6.57 (d, *J* = 15, 1H), 7.04–7.72 (m, 7H), 8.80 (d, *J* = 15, 1H). MALDI-TOF MS found: 1,600–2,300.

Synthesis of MRP3. To a solution of CyOH (23.40 mg, 0.05 mmol) in CH_3CN (10 ml) were added Br-Ph-DVED (0.13 g, 0.15 mmol) and *N*,*N*-diisopropylethylamine (79 µl, 0.62 mmol). After the reaction mixture was stirred at 70 °C for 4 h, it was poured into H_2O, extracted by CH_2Cl_2 and concentrated under a vacuum to yield the product. Trifluoroacetic acid (1 ml) and CH_2Cl_2 (2 ml) were added to the residue, and stirred for additional 30 min at 25 °C before conducting concentration under a vacuum. Further purification by preparative HPLC gave CC as a blue solid (49 mg, 91%). ^{1}H NMR (300 MHz, CD_3OD): δ 1.22 (s, 12H), 1.53 (m, 2H), 1.76 (m, 4H), 1.92 (t, 6H), 2.10 (t, 2H), 2.35 (t, 2H), 2.66 (m, 5H), 3.00 (m, 2H), 3.36 (m, 2H), 3.95 (t, 1 H), 4.26 (t, 2H), 4.58 (t, 1H), 5.19 (m, 3H), 6.42 (d, *J* = 15 Hz, 2H), 6.97 (s, 2H), 7.35 (m, 4H), 7.63(m, 4H), 8.67 (d, *J* = 15 Hz, 2H). ESI-MS (*m*/*z*): calcd: 1,072.48, found: 1,072.47. Compound CC (22 mg, 0.02 mmol) and propynyl-HPβCD (32 mg, 0.02 mmol) was dissolved in DMSO/H_2O (3 ml/3 ml). A solution of sodium ascorbate (4.10 mg, 0.02 mmol) and $CuSO_4{\cdot}5H_2O$ (8.30 mg, 0.033 mmol) in H_2O was added. After the mixture was stirred at 25 °C under a nitrogen atmosphere in the dark for 5 h, precipitation was conducted in acetone. Further purification by preparative HPLC gave MRP3 (45 mg, 84% yield) as a blue solid. ^{1}H NMR (300 MHz, D_2O): δ 1.21 (m, 16H), 1.48–1.74 (m, 8H), 2.12–2.32 (m, 6H), 2.38 (s, 2H), 3.02 (m, 3H), 3.25–4.25 (m, 51H), 4.32–4.55 (m, 5H), 5.15–5.32 (m, 9H), 6.17 (d, *J* = 12, 1H), 6.40 (d, *J* = 9, 1H), 7.03–8.66 (m, 12H). MALDI-TOF MS found: 2,350–2,850.

Synthesis of CP2 and CP5. To a mixture of CyOH (9.40 mg, 0.02 mmol) and methoxy-PEG-alkyne (MW: 2,000 or 5,000, 1.5 equiv. to CyOH) in DMSO/H_2O (2 ml/2 ml) was added a solution of sodium ascorbate (1.05 mg, 0.005 mmol) and $CuSO_4{\cdot}5H_2O$ (1.06 mg, 0.004 mmol) in H_2O. After the mixture was stirred at 25 °C under a nitrogen atmosphere in the dark for 5 h, it was precipitated in acetone.

Further purification by preparative HPLC gave CP2 (41 mg, 81% yield) and CP5 (92 mg, 83%) as a blue solid. ^{1}H NMR of CP2 (300 MHz, D_2O): δ 1.60–1.82 (m, 8H), 1.83 (m, 2H), 2.48 (m, 4H), 3.37 (m, 2H), 3.4–4.0 (m, 177H), 4.54 (t, 4H), 6.00–8.21 (m, 10H). ^{1}H NMR of CP5 (300 MHz, D_2O): δ 1.51 (m, 6H), 1.83 (m, 4H), 2.43 (s, 4H), 3.25–4.25 (m, 200H), 4.16–4.30 (m, 4H), 5.63–7.94 (m, 10H). MALDI-TOF MS found: 1,400–3,000 and 4,000–7,000 for CP2 and CP5, respectively.

Synthesis of CCD. CyOH (46.70 mg, 0.1 mmol), propynyl-HPβCD (0.20 g, 0.125 mmol), sodium ascorbate (4.60 mg, 0.022 mmol) and $CuSO_4{\cdot}5H_2O$ (7.50 mg, 0.03 mmol) were dissolved in DMSO/H_2O (3 ml/3 ml) and stirred at 25 °C under a nitrogen atmosphere in the dark for 5 h. Then the reaction was precipitated in acetone. Further purification by preparative HPLC afforded CCD (0.22 g, 86%) as a blue solid. ^{1}H NMR (300 MHz, D_2O): δ 1.23 (s, 18H), 1.85 (s, 6H), 1.99 (m, 6H), 2.72 (m, 2H), 3.05 (t, 2H), 3.25–4.25 (m, 74H), 4.34 (t, 1H), 4.57 (t, 2H), 5.18 (m, 9H), 5.62 (t, 2H), 6.59–7.72 (m, 10H). MALDI-TOF MS found: 1,600–2,180.

Synthesis of compound 5. A mixture of 3-hydroxybenzaldehyde (compound 4, 2.44 g, 20 mmol), trimethyl orthoformate (3.58 ml, 32 mmol) and tetrabutylammonium tribromide (0.49 g, 1.0 mmol) in methanol (30 ml) was stirred at 25 °C under a nitrogen atmosphere for 16 h. The reaction mixture was concentrated under a vacuum to remove methanol, then poured into saturated $NaHCO_3$ aqueous solution, extracted with EA, and concentrated under a vacuum. Purification of the residue by silica gel column chromatography gave compound 5 (3.20 g, 95% yield) as a colourless oil. TLC (silica gel, EA/PE = 1/5), R_f = 0.42. ^{1}H NMR (300 MHz, $CDCl_3$): δ 3.37 (s, 6H), 5.39 (s, 1H), 6.17 (s, 1H), 6.83 (m, 1H), 7.02 (m, 2H). ESI-MS (m/z): calcd: 168.08, found: 168.21.

Synthesis of compound 6. A mixture of 3-hydroxybenzaldehyde dimethyl acetal (compound 5, 2.52 g, 15.0 mmol), imidazole (1.53 g, 22.5 mmol) and *tert*-butyldimethylsilyl chloride (2.70 g, 18.0 mmol) in CH_2Cl_2 (20 ml) was stirred at 25 °C. After 16 h, the white precipitate was filtered off and the solvent was evaporated under a vacuum. Purification of the residue by silica gel column chromatography gave compound 6 (3.85 g, 91% yield) as a colourless oil. TLC (silica gel, EA/PE = 1/15), R_f = 0.45. ^{1}H NMR (300 MHz, $CDCl_3$): δ 0.23 (s, 6H), 1.02 (s, 9H), 3.36 (s, 6H), 5.38 (s, 1H), 6.82 (d, J = 3 Hz, 1H), 6.97 (s, 1H), 7.06 (d, J = 9 Hz, 1H), 7.30 (m, 1H). ESI-MS (m/z): calcd: 282.17, found: 282.30.

Synthesis of compound 7. Acetal (compound 6, 3.38 g, 12.0 mmol) and trimethyl phosphite (2.13 ml, 18.0 mmol) were dissolved in CH_2Cl_2 (40 ml) and stirred in an ice bath. Titanium (IV) chloride ($TiCl_4$) (2.38 ml, 18.0 mmol) was dropwise added and stirred for 16 h. The solution was poured into a saturated $NaHCO_3$ aqueous solution in the ice bath. After stirring for 15 min, the mixture was extracted by CH_2Cl_2 and concentrated under a vacuum to yield crude product, which was purified by silica gel column chromatography to give compound 7 (3.24 g, 75% yield) as a colourless oil. TLC (silica gel, EA/PE = 2/1), R_f = 0.52. ^{1}H NMR (300 MHz, $CDCl_3$): δ 0.21 (s, 6H), 0.99 (s, 9H), 3.38 (s, 3H), 3.69 (t, 6H), 4.48 (d, J = 15 Hz, 1H), 6.81 (d, J = 9 Hz, 1H), 6.94 (s, 1H), 7.01 (d, J = 6 Hz, 1H), 7.24 (m, 1H). ESI-MS (m/z): calcd: 360.15, found: 360.81.

Synthesis of compound 8. Phosphonate (compound 7, 3.24 g, 9.0 mmol) was dissolved in anhydrous THF (20 ml) under a nitrogen atmosphere at −78 °C. To the above solution, lithium di-isopropyl amide (2.0 M in THF, 6 ml, 10.35 mmol) was added and the solution was stirred for 0.5 h. 2-adamantanone (1.62 g, 10.8 mmol) in anhydrous THF (20 ml) was added and stirred for 0.5 h min at −78 °C, and then at 25 °C for an additional 3 h. The reaction mixture was poured into brine, extracted with EA and concentrated under a vacuum. Purification of the residue by silica gel column chromatography gave compound 8 (2.94 g, 85% yield) as a colourless oil. TLC (silica gel, EA/PE = 1/15), R_f = 0.65. ^{1}H NMR (300 MHz, $CDCl_3$): δ 0.20 (s, 6H), 0.98 (s, 9H), 1.78–1.97 (m, 13H), 3.25 (s, 1H), 3.38 (s, 3H), 6.75 (m, 2H), 6.79 (d, J = 3 Hz, 1H), 7.20 (t, 1H). ESI-MS (m/z): calcd: 384.25, found: 384.40.

Synthesis of compound 9. Compound 8 (2.94 g, 6.8 mmol) and tetra-butylammonium fluoride (1.0 M in THF, 7.5 ml, 7.5 mmol) were dissolved in anhydrous THF (30 ml) and stirred for 12 h at 25 °C. The reaction mixture was poured into diluted hydrogen chloride (HCl) aqueous solution, extracted with EA and concentrated under a vacuum. Purification of the residue by silica gel column chromatography afforded compound 9 (1.74 g, 95% yield) as a white solid. TLC (silica gel, EA/PE = 1/15), R_f = 0.30. ^{1}H NMR (300 MHz, $CDCl_3$): δ 1.79–1.97 (m, 12H), 2.65 (s, 1H), 3.25 (s, 1H), 3.33 (s, 3H), 5.58 (s, 1H), 6.80 (m, 1H), 6.86 (t, 2H), 7.22 (t, 1H). ESI-MS (m/z): calcd: 270.16, found: 270.18.

Synthesis of compound 10. To a solution of compound 9 (1.70 g, 6.3 mmol) in toluene (150 ml) was added *N*-iodosuccinimide (1.42 g, 6.3 mmol) in an ice bath and stirred at 25 °C for 12 h. The mixture was poured into saturated sodium thiosulfate ($Na_2S_2O_3$) aqueous solution, extracted with EA and concentrated under a vacuum. Purification of the residue by silica gel column chromatography gave compound 10 (1.97 g, 80% yield) as a white solid. TLC (silica gel, EA/PE = 1/5), R_f = 0.70. ^{1}H NMR (300 MHz, $CDCl_3$): δ 1.77–1.95 (m, 12H), 2.62 (s, 1H), 3.22 (s, 1H), 3.29 (s, 3H), 5.27(s, 1H), 6.63 (d, J = 3, 1H), 6.94 (s, 1H), 7.59 (d, J = 9, 1H). ESI-MS (m/z): calcd: 396.06, found [M-I]: 269.10.

Synthesis of CL. To a mixture of iodophenol (compound 10, 1.78 g, 4.5 mmol), methyl acrylate (1.16 g, 13.5 mmol) and triethylamine (0.68 g, 6.75 mmol) in anhydrous CH_3CN (30 ml) were added palladium acetate ($Pd(OAc)_2$) (50.50 mg, 0.225 mmol) and tri(*o*-tolyl)phosphine ($P(o\text{-tol})_3$) (13.70 mg, 0.045 mmol). The flask was sealed and the reaction was stirred at 90 °C for 12 h. Then the reaction mixture was poured into saturated ammonium chloride (NH_4Cl) aqueous solution, extracted with EA and concentrated under a vacuum. Purification of the residue by silica gel column chromatography gave CL (1.27 g, 80% yield) as a pale-yellow solid. TLC (silica gel, EA/PE = 1/1), R_f = 0.50. ^{1}H NMR (300 MHz, $CDCl_3$): δ 1.79–1.96 (m, 12H), 2.69 (s, 1H), 3.23 (s, 1H), 3.33 (s, 3H), 3.81 (s, 3H), 6.38 (s, 1H), 6.58 (d, J = 18 Hz, 1H), 6.86 (s, 2H), 7.41 (d, 1H), 7.95 (d, J = 18 Hz, 1H). ESI-MS (m/z): calcd $[M+H]^+$: 355.18, found: 355.15.

Synthesis of compound 11. Compound CL (1.27 g, 3.6 mmol) and anhydrous pyridine (10 ml) were stirred in anhydrous CH_2Cl_2 (15 ml) at −78 °C under a nitrogen atmosphere. Trifluoromethanesulfonic anhydride (1.22 ml, 7.2 mmol) was dropwise added with continuous stirring at −78 °C for 0.5 h and then at 25 °C for an additional 2 h. The reaction was quenched by saturated $NaHCO_3$ aqueous solution at 25 °C, extracted by EA. The organic layer was washed three times with diluted HCl and concentrated under a vacuum. Purification of the residue by silica gel column chromatography gave compound 11 (1.58 g, 90% yield) as a pale-yellow solid. TLC (silica gel, EA/PE = 1/6), R_f = 0.60. ^{1}H NMR (300 MHz, $CDCl_3$): δ 1.81–1.99 (m, 12H), 2.69 (s, 1H), 3.26 (s, 1H), 3.33 (s, 3H), 3.84 (s, 3H), 6.49 (s, J = 15 Hz, 1H), 7.32 (t, 2H), 7.66 (d, J = 9 Hz, 1H), 7.84 (d, J = 18 Hz, 1H). ESI-MS (m/z): calcd $[M+H]^+$: 487.13, found: 487.09.

Synthesis of compound 12. Compound 11 (1.50 g, 3.08 mmol) and sodium hydroxide (NaOH, 0.25 g, 6.16 mmol) were dissolved in THF (20 ml) and H_2O (5 ml). The reaction mixture was stirred at 60 °C for 4 h and monitored by TLC. On completion, the mixture was washed with diluted HCl, extracted with EA and evaporated under a vacuum. Purification of the residue by silica gel column chromatography gave compound 12 (1.38 g, 95% yield) as a pale-yellow solid. TLC (silica gel, EA/PE = 1/1), R_f = 0.42. ^{1}H NMR (300 MHz, CD_3OD): δ 1.76–1.92 (m, 12H), 2.69 (s, 1H), 3.22 (s, 1H), 3.25 (s, 3H), 6.54 (d, J = 18 Hz, 1H), 7.23 (s, 1H), 7.35 (d, J = 9 Hz, 1H), 7.74–7.86 (m, 2H). ESI-MS (m/z): calcd: 472.12, found: 472.16.

Synthesis of CSCL. Compound 12 (1.30 g, 2.75 mmol) and methylene blue (32 mg, 0.1 mmol) were dissolved in a mixture of CH_2Cl_2 and methanol (10 ml/10 ml). Oxygen was bubbled through the solution while irradiating with yellow light for 120 min. The reaction mixture was concentrated under a vacuum in a water bath with the temperature below 28 °C. Purification of the crude product by preparative HPLC afforded CSCL (0.83 g, 60% yield) as a white solid. ^{1}H NMR (300 MHz, $CDCl_3$): δ 0.86 (t, 1H), 1.25 (s, 1H), 1.75–1.92 (m, 10H), 2.92 (s, 1H), 3.26 (s, 3H), 6.32 (d, J = 9 Hz, 1H), 7.19 (s, J = 6 Hz, 1H), 7.37–7.65 (m, 3H). ESI-MS (m/z): calcd: 504.11, found: 504.20.

Synthesis of Cy7NH2. CyCl (0.26 g, 0.4 mmol) and *N*-Fmoc-1,3-diaminopropane hydrochloride (0.33 g, 1.0 mmol) were dissolved in DMF (10 ml) and stirred at 65 °C for 4 h. After cooling down, the mixture was poured into H_2O, extracted using CH_2Cl_2, and concentrated under a vacuum to yield crude product compound 13 as a blue solid. A mixture of compound 13 and piperidine (1 ml) in CH_2Cl_2 (4 ml) was stirred at 25 °C for 60 min. After that, it was poured into H_2O, extracted by using CH_2Cl_2 and concentrated under a vacuum. Purification of the crude product by silica gel column chromatography afforded Cy7NH2 (0.15 g, 55% yield) as a blue solid. TLC (silica gel, CH_2Cl_2/methanol = 15/1), R_f = 0.46. ^{1}H NMR (300 MHz, $CDCl_3$): δ 1.62 (m, 12H), 1.86 (m, 12H), 2.47 (t, 4H), 3.09 (t, 4H), 3.35 (m, 4H), 3.81–3.95 (m, 4H), 5.54 (d, J = 12 Hz, 2H), 6.79–6.87 (m, 4H), 7.24(m, 2H), 7.64 (m, 4H). ESI-MS (m/z): calcd: 687.46, found: 687.50.

Synthesis of CySCL. A mixture of Cy7NH2 (0.14 g, 0.2 mmol), CSCL (0.11 mg, 0.2 mmol), *N,N*-diisopropylethylamine (12.90 mg, 0.1 mmol) and (2-(1H-benzotriazol-1-yl)-1,1,3,3-tetramethyluronium hexafluorophosphate (0.15 g, 0.4 mmol) in DMF (6 ml) was stirred at 25 °C for 4 h. The reaction was poured into H_2O, extracted by CH_2Cl_2 and concentrated under a vacuum. Purification of the crude product by silica gel column chromatography gave CySCL (0.18 g, 75% yield) as a blue solid. TLC (silica gel, CH_2Cl_2/methanol = 15/1), R_f = 0.65. ^{1}H NMR (300 MHz, $CDCl_3$): δ 0.92 (m, 1H), 1.25 (s, 1H), 1.60–2.06 (m, 34H), 2.48 (m, 4H), 2.90 (t, 1H), 3.29 (s, 3H), 3.31 (m, 4H), 3.39 (m, 4H), 3.82–3.94 (m, 4H), 5.59 (d, J = 9 Hz, 2H), 6.29 (t, 1H), 6.83 (m, 3H), 7.03 (m, 3H), 7.23 (m, 2H), 7.29 (m, 2H), 7.38 (m, 3H), 7.54 (m, 1H), 7.70 (m, 1H). ESI-MS (m/z): calcd: 1,173.56, found: 1,173.40.

Synthesis of MRP$_D$. A mixture of CySCL (0.18 g, 0.15 mmol), propynyl cyclodextrin (0.60 g, 0.375 mmol), sodium ascorbate (6.80 mg, 0.033 mmol) and $CuSO_4{\cdot}5H_2O$ (8.30 mg, 0.033 mmol) in a solution of DMSO/H_2O (5 ml/5 ml)

was stirred in an ice bath under a nitrogen atmosphere in the dark for 5 h. Then the mixture was precipitated in acetone. Purification of the crude product by preparative HPLC gave a blue solid MRP_D (0.52 g, 80% yield). ^1H NMR (300 MHz, D_2O): δ 0.90 (m, 1H), 1.26 (s, 21H), 1.64–2.10 (m, 34H), 2.58 (m, 4H), 2.83 (t, 2H), 3.20 (m, 4H), 3.25–4.25 (m, 100H), 4.24 (t, 4H), 4.37 (t, 2H), 4.48 (t, 2H), 5.00–5.16 (m, 14H), 5.65 (t, 2H), 6.86–7.11 (m, 10H), 7.47–7.79 (m, 6H). MALDI-TOF MS found: 3,400–4,400.

Preparation of stock solutions. The MRPs and the uncaged fluorophores (CMe, CP2, CP5 and CCD) were dissolved in PBS (10 mM, pH 7.4) to obtain stock solutions. 10% DMSO/PBS are co-solvents for CMe. Stock solutions of H_2O_2, HOCl and $O_2^{\bullet-}$ were prepared by directly diluting H_2O_2, NaOCl and KO_2, respectively. $^1O_2$ was generated by addition of NaOCl to H_2O_2. $ONOO^-$ was generated from 3-morpholinosydnonimine hydrochloride. •OH was prepared by Fenton reaction between H_2O_2 and $Fe(ClO_4)_2$. Stock solutions of histidine, GSH, NAC, AA, HQ, caspase-3, furin, nitroreductase, βGal, FAPα, AAP, NAG, NaCl, KCl, $MgSO_4$, $CaCl_2$ and $FeSO_4$ were prepared with distilled water.

Optical measurement. MRP1, MRP2, MRP3 and MRP_D solutions (30 μM) were incubated with their respective biomarkers (60 μM KO_2, 40 mU NAG, 0.5 μg caspase-3 and 60 μM KO_2, respectively) in PBS (10 mM, pH 7.4) at 37 °C. Ultraviolet–visible absorption and fluorescence spectra of the solutions were measured on ultraviolet–visible and fluorescence spectrophotometers after 60 min incubation. Fluorescence images were acquired using the IVIS spectrum imaging system with excitation at 675 ± 10 nm (640 ± 10 nm for MRP_D) and emission at 720 ± 10 nm (760 ± 10 nm for MRP_D) and an acquisition time of 0.1 s. Chemiluminescence images were acquired under bioluminescence mode with an open filter and an acquisition time of 1 s. The sensing capability of MRPs was analysed through HPLC. Ultraviolet–visible absorption and fluorescence spectra of the uncaged fluorophores solution (30 μM) in PBS (10 mM, pH 7.4) were recorded on ultraviolet–visible and fluorescence spectrophotometers.

In vitro selectivity studies. MRP1 and MRP_D (30 μM) were treated with the indicated ROS (150 μM) and other analytes (150 μM) in PBS (10 mM, pH 7.4) at 37 °C for 60 min. MRP2 and MRP3 (30 μM) were incubated with the indicated ROS (150 μM), metal ions (150 μM), and enzymes including caspase-3 (0.5 μg) in PBS (10 mM, 0.1% Chaps, 50 mM NaCl, 5% glycerol, 10 mM EDTA, 1 mM dithiothreitol, pH 7.4), AAP (1.0 U) in HEPES buffer (10 mM, pH 7.4), furin (40 mU) in Tris buffer (25 mM, 0.5% (w/v) Brij-35, 1 mM $CaCl_2$, pH 9.0), nitroreductase (1.0 U) in Tris buffer (10 mM, 1 mM NADH, 1 mM K_2CrO_4, pH 7.0), plasmin (1.0 U) in lysine buffer (100 mM, pH 7.5), βGal (1.0 U) in acetate buffer (10 mM, pH 4.5), FAPα (0.9 U) in HEPES buffer (50 mM, 1 mg ml^{-1} BSA, 5% glycerol, pH 7.4), or NAG (40 mU) in PBS (10 mM, pH 7.4) at 37 °C for 60 min. Fluorescence or chemiluminescence enhancement of MRPs was measured on a fluorescence spectrophotometer or spectramax after incubation. Unit definition: 1 U of enzyme will hydrolyse 1 μmol of the corresponding substrate per minute under optimized conditions. PBS was purged with nitrogen gas for 35 min before these experiments.

Measurement of the LOD. The fluorescence intensities (720 nm) of MRP1 (30 μM) and chemiluminescence intensities (540 nm) of MRP_D (30 μM) were measured following addition of aliquots of micromolar concentration of KO_2. The LOD was calculated using the equation[46]: $LOD = 3\sigma/k$, where σ represents the standard deviation of emission intensities of the blank, and k represents the slope of the plot of emission intensities against the concentration of KO_2.

Enzyme kinetic assay. Various concentrations of MRP2 (5, 10, 15, 20, 25, 30, 35, 40, 45, 50 or 55 μM) or MRP3 (5, 10, 15, 20, 30, 40, 50 or 60 μM) were incubated with NAG (40 mU) or caspase-3 (0.5 μg) at 37 °C for 15 min in PBS (10 mM, pH 7.4). After incubation, the mixtures were analysed using HPLC for quantification. The initial reaction velocity (nM s^{-1}) was calculated, plotted against the concentration of MRP2 or MRP3, and fitted to a Michaelis–Menten curve. The kinetic parameters were calculated by use of the Michaelis–Menten equation[47]: $V = V_{max}*[S]/(K_m+[S])$, where V is the initial velocity and $[S]$ is substrate concentration.

Measurement of fluorescence quantum yields. Indocyanine green was used as a standard with a known fluorescence quantum yield (Φ) value of 13% in DMSO[48]. Fluorescence quantum yields were calculated using the following equation: $\Phi_s/\Phi_f = (A_s/A_f) \times (Abs_s/Abs_f) \times (\eta_s^2/\eta_f^2)$, where Φ_s and Φ_f are the fluorescence quantum yields of the standard and the samples, respectively; A_s and A_f are the emission areas of the standard and the samples, respectively; Abs_s and Abs_f are the absorbance of the standard and the samples at the wavelength of excitation; η_s and η_f are the refractive indices of the standard and the samples, respectively.

Determination of chemiluminescence kinetic profiles. MRP_D solution (30 μM) in PBS (10 mM, pH 7.4) was placed into the wells of a black 96-well plate. Chemiluminescence intensities were continuously acquired after addition of KO_2 (60 μM) using a spectramax. The chemiluminescence intensities were plotted as a function of time.

Tissue-penetration studies. MRP_D solution (30 μM) in PBS (10 mM, pH 7.4) was placed into the wells of a black 96-well plate. Chicken tissues with the desired thickness were overlaid on top of the wells. Chemiluminescence images were acquired after addition of KO_2 (60 μM) using the IVIS spectrum imaging system under bioluminescence mode with an open filter and an acquisition time of 180 s. Fluorescence images were acquired with excitation at 640 ± 10 nm and emission at 760 ± 10 nm and an acquisition time of 0.1 s. The SBR was calculated as SBR = fluorescence intensities (or chemiluminescence intensities)/background, where background is the signal intensity of neighboring tissues obtained over the imaging period[49]. The SBRs were plotted as a function of tissue depth.

In vivo biodistribution studies. All animal studies were conducted in accordance with the guidelines set by the Institutional Animal Care and Use Committee, Sing Health. Female nude mice (Tac:Cr:(NCr)-Fox1nu, 8 weeks old) and Balb/c mice (10 weeks old) were purchased from InVivos (Singapore). Aged female nude mice (25 weeks old) were obtained by feeding after receipt at 8 weeks old. NCr nude mice were i.v. injected with 0.2 ml saline (control), the uncaged fluorophores (CMe, CP2, CP5 and CCD, 8 μmol kg^{-1} body weight) or MRP_D (32 μmol kg^{-1} body weight), and imaged using the IVIS spectrum imaging system at 30 and 60 min post-injection. The abdominal cavity and resected organs from mice were imaged after euthanization at 60 min post-injection. Fluorescence images were acquired using the IVIS spectrum imaging system with excitation at 675 ± 10 nm (640 ± 10 nm for MRP_D) and emission at 720 ± 10 nm (760 ± 10 nm for MRP_D).

Pharmacokinetic studies. NCr nude mice were anesthetized by i.p. injection of ketamine/xylazine (ketamine: 50 mg kg^{-1} body weight; xylazine: 5 mg kg^{-1} body weight) for the entire duration of the experiment. The end of the tail was cut for blood extraction. Blood was sampled in heparinized capillary tubes as a reference before injection. Mice were i.v. injected with the uncaged fluorophores (CP2, CP5 and CCD, 8 μmol kg^{-1} body weight), MRPs1–3 (8 μmol kg^{-1} body weight) or MRP_D (32 μmol kg^{-1} body weight) and blood was sampled at 1, 4, 9, 16, 25, 35, 55 and 75 min post-injection. For pharmacokinetic studies of MRPs1–3 and MRP_D in cisplatin-treated mice, blood was sampled from living mice after 1, 4, 9, 16, 25, 35, 55, 75, 95 and 120 min injection of MRPs1–3 (8 μmol kg^{-1} body weight) or MRP_D (32 μmol kg^{-1} body weight) at different time points post-treatment with cisplatin (8, 12, 16, 48 or 72 h). Collected blood samples were stored in an ice box to prevent clotting before centrifugation at 3,500 r.p.m for 20 min. The uncaged fluorophores and MRPs were quantified using HPLC. Quantification results were presented as a bi-exponential decay curve to estimate elimination ($t_{1/2\beta}$) blood half-life values.

Renal clearance efficiency studies. NCr nude mice were i.v. injected with the uncaged fluorophores (CMe, CP2, CP5 and CCD, 8 μmol kg^{-1} body weight), MRPs1–3 (8 μmol kg^{-1} body weight) or MRP_D (32 μmol kg^{-1} body weight) and placed in metabolic cages. For renal clearance efficiency studies of MRPs1–3 in cisplatin-treated mice, mice were i.v. injected with MRPs1–3 (8 μmol kg^{-1} body weight) at t = 8, 12, 16, 48 or 72 h post-treatment with cisplatin (20 mg kg^{-1} body weight) and placed in metabolic cages. Urine was collected at 1, 3, 6, 9 and 24 h post-injection, centrifuged at 4,500 r.p.m. for 8 min and filtered by a 0.22 μm syringe filter. Excretion of the uncaged fluorophores and MRPs in the urine was quantified using HPLC. Mice were euthanized to image resected organs after 24 h urine collection. Major organs were collected, homogenized in PBS (10 mM, pH 7.4) and centrifuged at 4,500 r.p.m for 15 min to remove insoluble components. Fluorescence intensities of the final supernatants were measured on a fluorescence spectrophotometer.

In vivo stability and biocompatibility studies. The collected urine in PBS (10 mM, pH 7.4) was measured on ultraviolet–visible and fluorescence spectrophotometers, imaged by the IVIS spectrum imaging system and analysed by HPLC as well as MALDI-TOF mass spectrometry. Heart, liver, spleen, lung and kidneys were collected from NCr nude mice after 24 h injection of CCD, MRPs1–3 (8 μmol kg^{-1} body weight) or MRP_D (32 μmol kg^{-1} body weight) and placed into 4% paraformaldehyde (PFA) for histological examination.

Establishment of drug-induced AKI models in living mice. Mice were randomly selected and treated with cisplatin (5 mg kg^{-1}, 10 mg kg^{-1} or 20 mg kg^{-1} body weight, i.p. injection), gentamicin (100 mg kg^{-1} body weight day^{-1}, i.p. injection) or diatrizoate (1,000 mg kg^{-1} body weight, i.v. injection, water deprivation for 24 h before treatment). The control groups were treated with saline (0.2 ml) or NAC (400 mg kg^{-1} body weight, i.v. injection) 30 min before cisplatin administration[50]. Body weights of all the mice were recorded during treatment. After drug administration, the weight of mice and signs of discomfort were monitored on a daily basis during the entire experiments (Supplementary Fig. 36). Imaging, blood and urine sampling were conducted at different time points post-treatment with drug. At the end, the mice were euthanized and major organs were placed into 4% PFA for histological examination.

Real-time in vivo NIRF and chemiluminescence imaging of drug-induced AKI in living mice. Real-time NIRF imaging was conducted every 30 min for 2.5 h after i.v. injection of MRPs1–3 (8 μmol kg^{-1} body weight) at t = 8, 12, 16,

24, 48 or 60 h post-treatment with cisplatin, or i.v. injection of MRPs1 and 2 (8 μmol kg^{-1} body weight) at t = 24, 36, 48 or 72 h post-treatment with gentamicin, or i.v. injection of MRPs1-2 (8 μmol kg^{-1} body weight) at t = 2, 8, 16 or 48 h post-treatment with diatrizoate. Real-time dual-channel imaging was conducted every 30 min for 2 h after i.v. injection of MRP_D (32 μmol kg^{-1} body weight) at t = 8, 12, 48 or 72 h post-treatment with cisplatin, or at t = 24, 36, 96 or 144 h post-treatment with gentamicin, or at t = 2, 8, 16 or 48 h post-treatment with diatrizoate. The control groups were treated with saline (0.2 ml), and the negative control was treated with NAC (400 mg kg^{-1} body weight, i.v. injection) 30 min before cisplatin administration. Fluorescence images were acquired using the IVIS spectrum imaging system with excitation at 675 ± 10 nm (640 ± 10 nm for MRP_D) and emission at 720 ± 10 nm (760 ± 10 nm for MRP_D) and an acquisition time of 0.1 s. Chemiluminescence images were acquired under bioluminescence mode with an open filter and an acquisition time of 180 s. Mice were euthanized after i.v. injection of MRPs1–3 or MRP_D at different time points post-treatment with saline or drugs. The abdominal cavity and resected organs from mice were imaged after euthanization. Major organs were placed into 4% PFA for histological examination.

Determination of GFR in drug-treated living mice. FITC–inulin (150 mg) was dissolved in 0.9% NaCl (3 ml) at 75 °C and dialysed in 0.9% NaCl (1,000 ml) at 25 °C for 24 h. Dialysed FITC–inulin (3.74 μl g^{-1} body weight)[51] was injected i.v. into living NCr nude mice at t = 8, 12, 16, 24 or 48 h post-treatment with cisplatin (20 mg kg^{-1} body weight), or at t = 24, 36, 48, 96 or 144 h post-treatment with gentamicin (100 mg kg^{-1} body weight day^{-1}), or at t = 2, 8, 16, 24 or 48 h post-treatment with diatrizoate (1,000 mg kg^{-1} body weight), or saline (0.2 ml)-treated mice. Blood (approximately 20 μl) was collected via tail vein at 3, 7, 10, 15, 35, 55 and 75 min post-injection of FITC–inulin, and then centrifuged for 20 min at 3,500 r.p.m. The serum sample (10 μl) was diluted with HEPES buffer (40 μl, 500 mM, pH 7.4) and fluorescence was measured using a spectramax with excitation at 485 nm and emission at 538 nm. Serum fluorescence data were presented as a two-component exponential decay curve using nonlinear regression. GFR was calculated according to the equation[51]: $GFR = I/(A/\alpha + B/\beta)$, where I is the amount of FITC–inulin delivered by the bolus injection, A and B are the y-intercept values of the two decay rates, and α and β are the decay constants for the distribution and elimination phases, respectively.

Online urinalysis. Urine samples were collected from living mice after i.v. injection of MRPs1–3 (8 μmol kg^{-1} body weight) at t = 8, 12, 16, 24, 48, 60 or 72 h post-treatment with cisplatin (10 mg kg^{-1} or 20 mg kg^{-1} body weight), or at t = 24, 36, 48, 72 or 144 h post-treatment with gentamicin (100 mg kg^{-1} body weight day^{-1}), or at t = 2, 8, 16, 24 or 48 h post-treatment with diatrizoate (1,000 mg kg^{-1} body weight), or saline (0.2 ml)-treated mice. The collected urine samples were centrifuged at 4,500 r.p.m. for 8 min, filtered by a 0.22 μm syringe filter, and measured on a fluorescence spectrophotometer. Fluorescence images were acquired using the IVIS spectrum imaging system with excitation at 675 ± 10 nm and emission at 720 ± 10 nm. Activated MRPs were analysed by HPLC.

Offline urinalysis. Urine samples were collected using metabolic cages from drug-treated mice at different time points post-treatment with drug. The collected urine samples were centrifuged at 4,500 r.p.m. for 8 min and filtered by a 0.22 μm syringe filter. MRPs1–3 solutions (30 μM) in PBS (10 mM, pH 7.4) were incubated with the urine (100 μl) at 37 °C, followed by fluorescence measurements on a fluorescence spectrophotometer after 2 h incubation. Urinary TFF3, osteopontin, NGAL, β2-Microglobulin, KIM-1 and clusterin levels were quantified using ELISA kits according to the manufacturer's protocol.

Blood analysis. Blood was collected from the tail vein in living NCr nude mice under isoflurane anaesthesia at t = 8, 12, 16, 24, 48 or 72 h post-treatment with cisplatin (20 mg kg^{-1} body weight), or at t = 24, 48, 72, 96 or 144 h post-treatment with gentamicin (100 mg kg^{-1} body weight day^{-1}), or at t = 2, 8, 16, 24 or 48 h post-treatment with diatrizoate (1,000 mg kg^{-1} body weight), or saline (0.2 ml)-treated mice. The collected blood samples were centrifuged for 20 min at 3,500 r.p.m. sCr, BUN and cyst C were determined using commercial kits according to the manufacturer′s protocol.

Specificity studies in living mice with local skin inflammation. NCr nude mice were intradermally injected with saline (15 μl) or LPS (5 μg in 15 μl PBS) on the left thigh[52], followed by i.v. injection of MRP2 (8 μmol kg^{-1} body weight) at 4 h post-treatment with saline or LPS. Real-time NIRF imaging of living mice was conducted using the IVIS spectrum imaging system. Urine was collected from a separate set of saline- or LPS-treated mice at 4 h post-treatment. The collected urine samples were centrifuged at 4,500 r.p.m. for 8 min and filtered by a 0.22 μm syringe filter. MRP2 solutions (30 μM) in PBS (10 mM, pH 7.4) were incubated with the urine (100 μl) at 37 °C, followed by fluorescence measurement after 2 h incubation. Sections of skin from the injection sites were resected after euthanasia for immunofluorescence staining. Note that such a low dosage of LPS does not induce organ injury[53].

Specificity studies in living mice with ANIT-induced liver injury. NCr nude mice were fasted overnight and intragastrically injected with olive oil (0.2 ml, control group) or ANIT (dissolved in olive oil, 75 mg kg^{-1} body weight)[24], followed by i.v. injection of MRPs1–3 (8 μmol kg^{-1} body weight) at 24 h or 48 h post-treatment with olive oil or ANIT. Real-time NIRF imaging of living mice was conducted using the IVIS spectrum imaging system. For online urinalysis, urine was collected from control or ANIT-treated living mice after i.v. injection of MRPs1–3 (8 μmol kg^{-1} body weight) at 48 h post-treatment with ANIT. For offline urinalysis, urine was collected from a separate set of control or ANIT-treated mice at 48 h post-treatment. The collected urine samples were centrifuged at 4,500 r.p.m. for 8 min and filtered by a 0.22 μm syringe filter. MRPs1–3 solutions (30 μM) in PBS (10 mM, pH 7.4) were incubated with the urine (100 μl) at 37 °C, followed by fluorescence measurement after 2 h incubation. Liver and kidneys were resected after euthanasia at 24 h or 48 h post-treatment with olive oil or ANIT for H&E and immunofluorescence staining. Note that ANIT does not induce kidney injury[24].

Histology. All tissues were fixed with 4% PFA, dehydrated in ethanol solution, embedded in paraffin and cut into sections with a thickness of 10 μm for H&E staining. The paraffin was removed by xylene washing and then the sections were incubated with haematoxylin for 4 min and eosin for 2 min, followed by washing with distilled water. The stained sections were examined using a Nikon ECLIPSE 80i microscope. For immunofluorescence staining, liver, heart, lung, skin, spleen and kidney tissues were fixed with 4% PFA, dehydrated using 30% sucrose solution, embedded in frozen optimal cutting temperature (O.C.T.) medium, and then cut into sections with a thickness of 10 μm (40 μm for the whole kidney sections). The sections were dried at 25 °C for 60 min, washed 3 times using PBS containing 0.1% Triton X-100, and incubated with 3% BSA solution at 25 °C for an additional 60 min, followed by PBS washing and incubation with the respective antibody (cleaved-caspase-3 antibody, anti-CD31 antibody or anti-CD11b antibody) for 60 min at 37 °C. After three washes with PBS to remove unbound antibody, the sections were counterstained with Alexa Fluor 488-conjugated goat anti-rabbit IgG H&L for 60 min at 25 °C. Next, the cell nuclei were stained with 4′,6-diamidino-2-phenylindole (DAPI). The stained sections were imaged using an LSM800 confocal laser scanning microscope.

Statistics and reproducibility. The in vivo and ex vivo fluorescence or chemiluminescence signals were quantified with region of interest analysis using Living Image 4.3 software. The data are mean ± standard deviation (s.d.) unless stated otherwise. Investigators were blinded to group allocation during experiments. Investigators performing in vivo imaging were blinded to saline and drug treatment groups. Statistical differences between two groups were tested with a two-tailed Student's t-test and more than three groups were determined by one-way analysis of variance followed by Tukey's post hoc test. For all tests, P values less than 0.05 were considered statistically significant; $^*P < 0.05$, $^{**}P < 0.01$ and $^{***}P < 0.001$. All statistical calculations were performed using GraphPad Prism 6.0, including assumptions of tests used.

Reporting Summary. Further information on research design is available in the Nature Research Reporting Summary linked to this article.

Data availability

The authors declare that all relevant data supporting the findings of this study are available within the article and in the Supplementary Information, or from the corresponding author on reasonable request.

References

46. Hu, J. J. et al. Fluorescent probe HKSOX-1 for imaging and detection of endogenous superoxide in live cells and in vivo. *J. Am. Chem. Soc.* **137**, 6837–6843 (2015).
47. Gu, K. et al. Real-time tracking and in vivo visualization of beta-galactosidase activity in colorectal tumor with a ratiometric near-infrared fluorescent probe. *J. Am. Chem. Soc.* **138**, 5334–5340 (2016).
48. Benson, R. C. & Kues, H. A. Absorption and fluorescence properties of cyanine dyes. *J. Chem. Eng. Data* **22**, 379–383 (1977).
49. Hyun, H. et al. Structure-inherent targeting of near-infrared fluorophores for parathyroid and thyroid gland imaging. *Nat. Med.* **21**, 192–197 (2015).
50. Dickey, D. T. et al. Effect of *N*-acetylcysteine route of administration on chemoprotection against cisplatin-induced toxicity in rat models. *Cancer Chemother. Pharmacol.* **62**, 235–241 (2008).
51. Qi, Z. et al. Serial determination of glomerular filtration rate in conscious mice using FITC–inulin clearance. *Am. J. Physiol. Renal Physiol.* **286**, F590–F596 (2004).
52. Medicherla, S. et al. Topical alpha-selective p38 MAP kinase inhibition reduces acute skin inflammation in guinea pig. *J. Inflamm. Res.* **3**, 9–16 (2010).
53. Wang, W. et al. Prostacyclin in endotoxemia-induced acute kidney injury: cyclooxygenase inhibition and renal prostacyclin synthase transgenic mice. *Am. J. Physiol. Renal Physiol.* **293**, F1131–F1136 (2007).

nature research

Corresponding author(s): Kanyi Pu

Reporting Summary

Nature Research wishes to improve the reproducibility of the work that we publish. This form provides structure for consistency and transparency in reporting. For further information on Nature Research policies, see Authors & Referees and the Editorial Policy Checklist.

Statistical parameters

When statistical analyses are reported, confirm that the following items are present in the relevant location (e.g. figure legend, table legend, main text, or Methods section).

n/a	Confirmed	
☐	☒	The exact sample size (*n*) for each experimental group/condition, given as a discrete number and unit of measurement
☐	☒	An indication of whether measurements were taken from distinct samples or whether the same sample was measured repeatedly
☐	☒	The statistical test(s) used AND whether they are one- or two-sided *Only common tests should be described solely by name; describe more complex techniques in the Methods section.*
☒	☐	A description of all covariates tested
☒	☐	A description of any assumptions or corrections, such as tests of normality and adjustment for multiple comparisons
☐	☒	A full description of the statistics including central tendency (e.g. means) or other basic estimates (e.g. regression coefficient) AND variation (e.g. standard deviation) or associated estimates of uncertainty (e.g. confidence intervals)
☐	☒	For null hypothesis testing, the test statistic (e.g. *F*, *t*, *r*) with confidence intervals, effect sizes, degrees of freedom and *P* value noted *Give P values as exact values whenever suitable.*
☒	☐	For Bayesian analysis, information on the choice of priors and Markov chain Monte Carlo settings
☒	☐	For hierarchical and complex designs, identification of the appropriate level for tests and full reporting of outcomes
☒	☐	Estimates of effect sizes (e.g. Cohen's *d*, Pearson's *r*), indicating how they were calculated
☐	☒	Clearly defined error bars *State explicitly what error bars represent (e.g. SD, SE, CI)*

Our web collection on statistics for biologists may be useful.

Software and code

Policy information about availability of computer code

Data collection	Shimadzu UV Probe software and fluorolog software were used to acquire UV, fluorescence and chemiluminescence data. Agilent openLab control panel was used to acquire HPLC data. MicroManager was used to acquire histological data. ZEN blue was used for confocal microscopy to acquire fluorescence images. Marvin and JChem calculator plug-ins was used to calculate the partition coefficients. Living Image Software was used for IVIS Imaging Systems to acquire fluorescence imaging data.
Data analysis	Imaging data were analyzed using the Living Image 4.3 Software (PerkinElmer). Confocal fluorescence microscopy imaging data were analyzed using Zen 2.3 blue edition (Carl Zeiss). All statistical calculations were performed using GraphPad Prism 6.0 (GraphPad Software Inc.). NMR spectra were analyzed using Mestre Nova LITE v5.2.5-4119 software (Mestre lab Research S.L.).

For manuscripts utilizing custom algorithms or software that are central to the research but not yet described in published literature, software must be made available to editors/reviewers upon request. We strongly encourage code deposition in a community repository (e.g. GitHub). See the Nature Research guidelines for submitting code & software for further information.

Data

Policy information about availability of data

All manuscripts must include a data availability statement. This statement should provide the following information, where applicable:

- Accession codes, unique identifiers, or web links for publicly available datasets
- A list of figures that have associated raw data
- A description of any restrictions on data availability

The authors declare that all relevant data supporting the findings of this study are available within the article and in the Supplementary Information document, or from the corresponding author on reasonable request.

Field-specific reporting

Please select the best fit for your research. If you are not sure, read the appropriate sections before making your selection.

☒ Life sciences ☐ Behavioural & social sciences ☐ Ecological, evolutionary & environmental sciences

For a reference copy of the document with all sections, see nature.com/authors/policies/ReportingSummary-flat.pdf

Life sciences study design

All studies must disclose on these points even when the disclosure is negative.

Sample size	G*power analysis was used to calculate and ensure the sample sizes fulfill adequate power (p>0.8). According to the experimental data and sample size (n) and P valuewere calculated and the power was then calculated. If it is more than 80%, demonstrating the sample size is adequate. All sample sizes, statistical tests and P values are indicated in the figure legends.
Data exclusions	No data was excluded from the analysis.
Replication	Experiments were repeated at least three independent experiments with similar results. All experiments were reproduced to reliably support conclusions stated in the manuscript.
Randomization	Cages of mice were randomly selected and then divided into experimental groups for further treatment.
Blinding	Investigators were blinded to group allocation during experiments. Investigators performing in vivo fluorescence imaging were blinded to saline and drug treatment groups. This information is included in the Methods section.

Reporting for specific materials, systems and methods

Materials & experimental systems

n/a	Involved in the study
☒	☐ Unique biological materials
☐	☒ Antibodies
☒	☐ Eukaryotic cell lines
☒	☐ Palaeontology
☐	☒ Animals and other organisms
☒	☐ Human research participants

Methods

n/a	Involved in the study
☒	☐ ChIP-seq
☒	☐ Flow cytometry
☒	☐ MRI-based neuroimaging

Antibodies

Antibodies used	Cleaved-caspase-3 antibody (Cell Signaling Technology, catalog# 9661L, polyclonal, dilution 1:500) Anti-CD31 antibody (Abcam, catalog# ab28364, polyclonal, dilution 1:500) anti-CD11b antibody (Abcam, catalog# ab133357, clone EPR1344, dilution 1:1000) and Alexa Fluor 488 conjugated goat anti-rabbit IgG H&L (Abcam, catalog# ab150077, polyclonal, dilution 1:500). All anti-body information are included in the Methods section.
Validation	All antibodies were used in the study according to the profile of manufacturers. Antibody validation for immunofluorescence was validated by the supplier and confirmed in Figure 4, Supplementary Figures 13, 15, 17, 34 and 35.

Animals and other organisms

Policy information about studies involving animals; ARRIVE guidelines recommended for reporting animal research

Laboratory animals	All animal studies were performed in compliance with the guidelines set by the Institutional Animal Care and Use Committee (IACUC), Sing Health. Female nude mice (Tac:Cr:(NCr)-Fox1nu, 8 weeks old) were obtained from InVivos Pte Ltd (Singapore). Aged female nude mice (25 weeks old) were obtained by feeding after receive at 8 weeks old. Female Balb/c mice (10 weeks old), male type 2 diabetic BKS-db mice (BKS-Leprem2Cd479 with a C57BLKS/J background, 12 weeks old) and male nondiabetic C57BLKS/J wild-type mice (12 weeks) were obtained from nanjing biomedical research institute of Nanjing University (Nanjing, China).
Wild animals	The study did not involve wild animals.
Field-collected samples	The study did not involve samples collected from the field.